Iron Isotopes Applied to BIF-Hosted Iron Deposits

Lydia Maria Lobato, Rosaline Cristina Figueiredo e Silva, Thomas Angerer, Mônica de Cássia Oliveira Mendes, and Steffen G. Hagemann

Abstract

Published and unpublished iron isotope data from banded iron formations (BIF) and their BIF-hosted hypogene (hydrothermal) iron ores from the Quadrilátero Ferrífero (itabirites), Corumbá, and Carajás iron districts in Brazil, as well as from the Hamersley province in Australia are presented and discussed. BIF constitutes a typically thinly bedded or laminated chemical sedimentary rock, with $\geq$ 15% Fe and layers of chert, chalcedony, jasper, or quartz, whereas itabirite is considered a laminated, metamorphosed iron formation rich in iron oxides, which may contain carbonate minerals, amphiboles, and abundant quartz. For the Paleoproterozoic Quadrilátero

L. M. Lobato (✉) · R. C. Figueiredo e Silva
Universidade Federal de Minas Gerais, Centro de Pesquisas Prof. Manoel Teixeira da Costa-Instituto de Geociências, Av. Antônio Carlos 6627, Campus Pampulha, Belo Horizonte, MG 31270-901, Brazil
e-mail: llobato.ufmg@gmail.com

T. Angerer
Institute of Mineralogy and Petrography, University of Innsbruck, Innrain 52, 6020 Innsbruck, Austria

M. de Cássia Oliveira Mendes
CDM—Centro de Desenvolvimento Mineral—Vale S.A, Santa Luzia, MG 33.040-900, Brazil

S. G. Hagemann
Centre for Exploration Targeting, School of Earth Sciences, University of Western Australia, Crawley, WA 6009, Australia

Ferrífero district, the range in δ^{56}Fe values of hypogene iron ores is similar to that of the metamorphosed BIFs, and iron isotope variations are better distinguished in different regional deformational domains. Light isotopic compositions dominate in the low deformation domain (δ^{56}Fe = -0.42 ± 0.12 to 0.29 ± 0.04‰), whereas the eastern, high-strain domain is characterized by heavy values (δ^{56}Fe = -0.09 ± 0.08 to 0.37 ± 0.06‰; Mendes et al., Mineral Deposita 52:159–180, 2017). Iron isotope composition for the Neoproterozoic iron formations of the Corumbá region (hematitic, dolomite-rich: -1.83 and -0.83‰; cherty-hematite: δ^{56}Fe -0.49‰) are controlled by: (1) primary seawater signature, (2) microbial activity, and (3) supergene goethite alteration. Hydrothermal alteration is reflected in the oxygen isotope data, but apparently not in the iron isotope fractionation. Iron and oxygen isotope pairing shows that δ^{56}Fe values increase, while δ^{18}O values decrease. In the Archean jaspilites of Carajás, hypogene ores tend to display lighter δ^{56}Fe values than their host BIF counterparts. Also, there is a correlation between coupled iron and oxygen isotope values that is clearer towards lighter isotopic values, especially for δ^{18}O. In the Paleoproterozoic Hamersley deposits, correlation between δ^{18}O and δ^{56}Fe values suggests a direct correlation of both isotope systems during low-grade, greenschist-facies metamorphism. On the other hand, despite the

evident shift to negative $\delta^{18}O$ values and apparent preservation of the metamorphic $\delta^{56}Fe$ signature, iron ore and hydrothermally modified BIF show a correlation between $\delta^{18}O$ and $\delta^{56}Fe$ values. In contrast, in supergene-modified samples a negative correlation is apparent. The Carajás (+1.24 to + 0.44; one sample − 0.30‰) and Hamersley (+ 1.02 to − 0.29‰) hypogene ores display $\delta^{56}Fe$ in a similar interval, reaching positive values, whereas ores from the Quadrilátero Ferrífero show a tendency towards lower values (to − 0.80‰). This review indicates that the application of iron isotopes in exploration is presently limited mainly due to the restricted dataset available for ore samples. Nevertheless, and despite all local differences, there is a general tendency for hypogene ores to display moderately lighter $\delta^{56}Fe$ values for all deposits compared to precursor BIF. In contrast, a strong supergene imprint in ore leads to moderately heavier $\delta^{56}Fe$ values. As more data become available, and if these trends are confirmed, the use of this tool may be valuable in the future, for instance to decipher the hypogene or supergene origin of specific ore zones, and as a consequence the probable depth extension or interpretation of concealed, deep orebodies.

Keyword

Iron isotopes · Iron deposits · Quadrilátero Ferrífero · Corumbá · Carajás · Hamersley

1   Introduction

Stable isotope geochemistry has become extensively applied to geosciences in the last decades, with applications in a wide range of geological processes, including mineral deposits (e.g., Horn et al. 2006; Shanks 2014). Since the development of the high-resolution mass spectrometers with multiple collectors (MC-ICP-MS), analysis of non-traditional stable isotopes, such as iron isotopes, has become possible. In particular, iron

isotope geochemistry is quite conspicuous because of its relatively high concentrations on Earth, making it a good tool for tracing the geochemical cycle of Fe (e.g., Johnson and Beard 2006; Dauphas et al. 2017).

Significant iron isotopic variability of natural materials is demonstrated by studies conducted in different geological environments (e.g., Levasseur et al. 2004; Williams et al. 2005b; Horn et al. 2006; Johnson and Beard 2006; Poitrasson 2006; Teng et al. 2008; Weyer 2008; Schoenberg et al. 2009; Xiaohu Li et al. 2017). Banded iron formations (BIF), for example, show a relatively large range in iron isotope compositions, varying from − 2.5 to + 2.2‰ in $\delta^{56}Fe$. In the study of BIF, these variations help discern iron sources and construct models for BIF genesis (e.g., Johnson et al. 2003, 2008a, b; Frost et al. 2007; Whitehouse and Fedo 2007; Fabre et al. 2011; Halverson et al. 2011; Planavsky et al. 2012; Czaja et al. 2013; Cox et al. 2016).

Despite the increase of iron isotope measurements for different geological settings, and for BIF themselves, there is little systematic application to hydrothermal BIF-hosted iron ores (e.g., Mendes et al. 2017). Examples include studies by Markl et al. (2006) of Fe-bearing minerals in the Variscan Schwarzwald hydrothermal vein deposits (Germany); magnetite in Kiruna-type (IOA Weis 2013; Weis et al. 2013; Bilenker 2015; Bilenker et al. 2016; Childress et al. 2016; Knipping et al. 2019; Troll et al. 2019); magnetite and sulfides in Archean Carajás IOCG deposits, Brazil (Santiago 2016); magnetite in the Chinese Xinqiao skarn deposit (Wang et al. 2011); and BIF-hosted magnetite ores of the Anshan-Benxi area in the North China craton (Dai et al. 2017). Limited data from hydrothermal iron deposits have shown that iron isotope ratios are partly controlled by hydrothermal fluid circulation (Horn et al. 2006; Markl et al. 2006), and by the hydrothermal mineralization conditions (Mendes et al. 2017).

The interaction of primary hematite with hydrothermal fluids in most cases enriches the lighter isotopes in the secondary hematite. For

siderite, isotopes fractionate in the opposite direction (Markl et al. 2006). Hydrothermal fluids therefore preferentially scavenge the light iron from iron-bearing minerals from surrounding rocks (e.g., Rouxel et al. 2003; Markl et al. 2006). Consequently, if a hydrothermal fluid percolates through protore BIF, the isotope composition of the hydrothermal fluid and its eventual ores are expected to be relatively lower in iron isotope values, whereas the residual BIF tends towards higher δ^{56}Fe ratios. Precipitation of Fe-bearing minerals results in the iron isotope composition of residual fluids evolving with time. Precipitation of Fe(III) minerals leaves the remaining fluid enriched in light isotopes, resulting in progressively lighter precipitates from the same fluid.

The complexity of isotopic fractionation during hydrothermal mineralization was emphasized by Horn et al. (2006). The isotopic composition suggests that fractionation can take place during the precipitation of iron phases, with variation of the δ^{56}Fe values even on the scale of a single hematite crystal (δ^{56}Fe = − 0.5‰, in the core and − 1.8‰, in the rim), reflecting the relative increase in content of the lighter isotope in the residual fluid (see also Steinhoefel et al. 2009).

Iron isotopes potentially identify precursors to hydrothermal alteration products and their associated ores. During hydrothermal processes, isotopic fractionation and isotopic composition of iron ore minerals may indicate iron sources (i.e., sedimentary, magmatic or metamorphic, or fluid evolution), allowing the reconstruction of precipitation and redox processes (Markl et al. 2006) that take place during ore formation and/or alteration.

This paper reviews and presents published iron isotope data from the Brazilian Quadrilátero Ferrífero (QF), Urucum (in Corumbá) and Carajás (jaspilite) iron districts (Fig. 1a–c). New data from Corumbá and Carajás, as well as from the Hamersley (Fig. 1d) province in Australia (BIF and iron ores), are presented. New and previously reported oxygen isotope results are also introduced for some of the samples in order to investigate the behavior and potential coupling with iron isotope. The main goal of this

contribution is to show the variation of iron isotopes from the protore BIF to their associated high-grade iron ores, as well as compare and contrast iron isotopes in the various iron ore districts. A brief review on iron isotope fractionation is included. Some future applications of iron isotope studies to mineral systems are suggested, with ideas about applying iron isotopes in the context of exploration.

2 Brief Summary on Iron Isotopes

In this section, we briefly review the most relevant information concerning iron fractionation in natural environments. Since the goal of this contribution is to evaluate how iron isotope variations take place during the hydrothermal upgrade of iron formations, the focus is directed mainly towards this latter subject.

Several reviews have been published over the past 15 years covering different aspects of iron isotope geochemistry (e.g., Beard and Johnson 2004; Johnson et al. 2004, 2008a; Dauphas and Rouxel 2006; Anbar and Rouxel 2007; Dauphas et al. 2017). In the present review, emphasis is given to the development of iron isotope systematics over the past decade, although still highlighting the important discoveries made before that time. The most important aspects in the past 10 years include the recognition that igneous rocks and minerals can display iron isotopic variations; a better understanding of the ancient iron marine cycle; and the first extensive use of iron isotope measurements in modern seawater to better understand the modern marine iron cycle. The past decade has also seen a large increase in the number of laboratory experiments aimed at determining equilibrium and kinetic fractionation factors needed to interpret iron isotope variations in natural samples.

Before examining iron isotope composition of iron ores, it is important to consider some aspects of the isotopic compositions of their protolith BIF. Iron is delivered to the depositional basins mainly through submarine hydrothermal vent fluids, with δ^{56}Fe composition being roughly –0.5 to 0.0‰ (Beard et al. 2003; Severmann
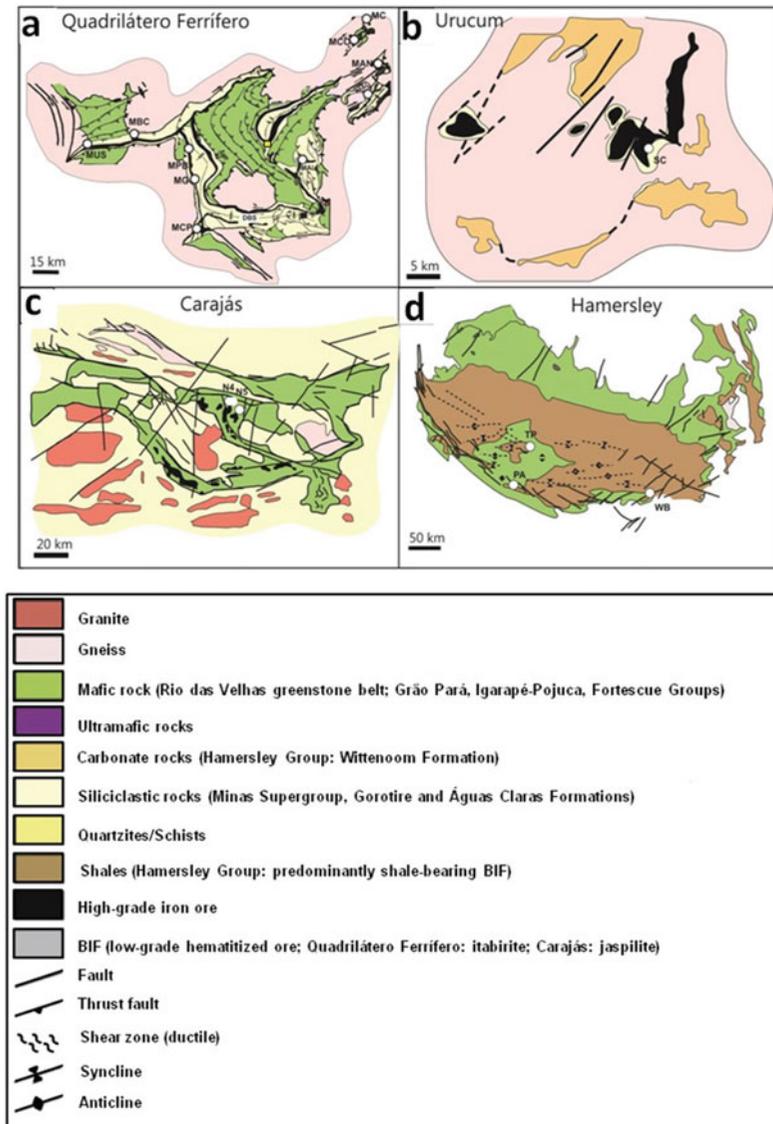
Fig. 1 Geological maps with sampling location for BIF-hosted iron ore districts and deposits (modified after Hagemann et al. 2016). **a** Quadrilátero Ferrífero (QF), Brazil (after Dorr 1969; Rosière et al. 2008). The open circles indicate locations of the Usiminas (MUS), Bocaina, (MBC), Pau Branco (MPB), Várzea do Lopes (MG), Casa de Pedra (MCP), Alegria (MAL), Morro Agudo (MAG), Andrade (MAN), Conceição (MCO), Cauê (MC) Mina de Fábrica (MF), and Dom Bosco Syncline (DBS) deposits. The yellow square indicates the southern Ouro Fino Syncline (OFS) portion of Gandarela Sycline (GS) (see Sampaio et al. 2018). **b** Urucum (Corumbá region), Brazil (after Walde and Hagemann 2007). Open circle with SC indicates the Santa Cruz deposit. **c** Serra Norte, Carajás mineral province, Brazil (after Figueiredo e Silva et al. 2008). Open circles indicate the N4 and N5 iron deposits. **d** Hamersley, Australia (after Angerer et al. 2012). Open cirlces indicate the TP Tom Price (TP), Paraburdoo (PA), and Whaleback (WB) deposits

et al. 2004; Johnson et al. 2008a). The deposition of iron oxides/hydroxides is influenced by the availability of oxygen in the ocean, which is reflected in the $\delta^{56}Fe$ signatures of iron formations (Johnson et al. 2008a; Planavsky et al. 2012). Quantitative oxidation of Fe(II) would

result in zero fractionation between the hydrothermal iron source and iron oxyhydroxide minerals. In contrast, partial Fe(II) oxidation produces ferric oxides with positive δ^{56}Fe values (Johnson et al. 2008b; Planavsky et al. 2012), with consequent depletion of the ferrous iron in the iron pool (Dauphas et al. 2004; Rouxel et al. 2005; Planavsky et al. 2012). Archean BIFs, for example, tend to have positive δ^{56}Fe signatures (Whitehouse and Fedo 2007; Fabre et al. 2011; Czaja et al. 2013; Busigny et al. 2014) due to non-quantitative fractionation in response to limited availability of free oxygen. Similar signatures are also observed for the Neoproterozoic BIFs deposited during glaciation episodes (Busigny et al. 2018). With the rise of atmospheric oxygen, during the Great Oxidation Event (GOE) at *ca.* 2.4 Ga (eg. Holland 2006 and references therein), the δ^{56}Fe signatures of Paleoproterozoic BIF become similar to values of the hydrothermal source due to quantitative fractionation of iron (see recent discussion in e.g., Lantink et al. 2018).

When considering the iron isotope fractionation, both biological and abiological mechanisms must be taken into account. The largest iron isotopic fractionations are associated with biologically mediated or abiologically induced, redox transformations between ferrous and ferric iron (Johnson et al. 2002, 2008b; Beard and Johnson 2004; Anbar et al. 2005). Mass-dependent Rayleigh-type fractionation may arise during progressive removal of relatively ^{56}Fe-enriched iron oxides from the iron reservoir, resulting in the relative enrichment of ^{54}Fe in the residual pool (Rouxel et al. 2005; Planavsky et al. 2012).

Biologically induced dissimilatory iron reduction (DIR) produces some of the largest natural fractionations of stable iron isotopes (Crosby et al. 2007). This mechanism is driven by a bacterial metabolic process, with transference of electrons to Fe-oxyhydroxides (Lovley et al. 2004). The DIR produces aqueous ferrous iron (Fe(II)$_{aq}$) that is isotopically up to $\sim$3‰ lighter than the ferric iron substrate (Beard et al. 1999, 2003; Johnson et al. 2005; Crosby et al. 2005, 2007; Kunzmann et al. 2017).

At higher temperatures, fractionation typical of hydrothermal fluids has been evaluated by experimental procedures through the investigation of the fractionation of iron between saline solutions and hematite (Saunier et al. 2011). These experiments demonstrate the absence of fractionation between fluid and precipitated hematite at 200 °C, and negative fractionation at even higher temperatures (Δ^{57}Fe$_{fluid-hematite} \approx -$0.5‰, at 300 °C), suggesting preferential transport of isotopically light iron at temperatures > 200ºC. At 800 °C, Sossi and O'Neil (2017) show that experimentally determined fractionation factors between minerals and aqueous FeCl$_2$ fluid have a minimal fractionation between ^{VI}Fe^{2+} and the fluid. If this represents speciation of iron in fluids exsolving from magmas, the fractionation between them should be small, unless the iron is hosted in magnetite, with both ferrous and ferric iron.

3 Geological Background of Selected Iron-Ore Districts

3.1 Quadrilátero Ferrífero

The Quadrilátero Ferrífero (QF) province (Fig. 1a), located in Minas Gerais state, plays a significant role in the Brazilian mining industry, hosting important gold and iron ore deposits, besides manganese and bauxite resources. The Minas Gerais iron ore corresponded to *ca*. 52% of the total Brazil´s iron ore exports in 2014 (177.675 t, IBRAM 2015 report, http://www.ibram.org.br/sites/1300/1382/00005836.pd).

Iron orebodies are hosted in Paleoproterozoic banded iron formations (BIF) of the regionally extensive Cauê Formation (Itabira Group, Minas Supergroup: Dorr 1969; Fig. 1 of Mendes et al. 2017). The Minas Supergroup consists of a platformal sedimentary succession, including clastic (Caraça, Piracicaba and Sabará groups) and chemical (Itabira Group) units metamorphosed to low greenschist facies (Dorr 1969). The metamorphosed and oxidized Cauê BIFs are commonly referred to as itabirites, and are composed predominantly of iron oxides

Fig. 2 Photomicrographs, illustrating examples of different types of iron ores from districts discussed in the text. **a** Massive iron ore, formed predominantly by anhedral(A) (± subhedral(S)) hematite, Pau Branco deposit, Quadrilátero Ferrífero (QF). **b** Specularite-bearing, schistose iron ore from a high-strain ore zone, Várzea do Lopes deposit, QF. **c** Sample of hematite mud with compact, laminated texture and local chert lenses. **d** Brecciated martite-hematite ore from the N4W deposit, Carajás, where microcrystalline hematite is preserved.

e Brecciated euhedral-tabular (ET) hematite ore from the ▶ N5E deposit, Carajás. **f** and **g** From Mt. Tom Price deposit, Hamersley province, the former showing aggregates of microplaty hematite (MpH) in high-grade ore, and the latter representing martite-microplaty hematite ore. Hem = hematite; Mt = martite; MHem = microcrystalline hematite; MpHem = microplaty hematite. Photomicrographs d, f, g taken under transmitted light; all others reflected light

(hematite, magnetite and martite, after magnetite) and quartz. Quartz itabirite is the most common, followed by calcareous (dolomite and ankerite, with minor calcite and siderite) and amphibolitic itabirites, the latter resulting from the metamorphism of calcareous itabirites (Rosière et al. 2008).

The QF region experienced important deformational events (e.g., Alkmim and Marshak 1998; Baltazar and Lobato 2020). The first was the Neoarchean Rio das Velhas event, followed by the 2.3–2.1 Ga Rhyacian-aged orogeny with the generation of NE-SW-trending fold and thrust belts verging to the NW. Then came the orogenic collapse at ca. 2.1 Ga (Alkmim and Marshak 1998). Finally, there was the Neoproterozoic Brasiliano orogeny, responsible for the formation of fold and thrust belts verging to the west (Alkmim and Marshak 1998), which imposed regional temperature and pressure gradients of 300–600 °C and 3–5 kbars, respectively, from west to east (Pires 1995). These tectono-metamorphic events resulted in a deformational and metamorphic gradient in the region that characterizes western, low-strain and eastern, high-strain domains, the latter most affected by Neoproterozoic tectonics (Rosière et al. 2001).

The evolution of the high-grade, hypogene ores is interpreted to have occurred synchronically to the Rhyacian-aged orogeny (2.03 Ga, Rosière et al. 2012), involving hydrothermal fluids of different origins and compositions, with formation of different generations of iron oxides (Rosière and Rios 2004; Rosière et al. 2008). During the first, contractional stage, reduced metamorphic fluids and oxidized connate water leached silica and carbonate from BIFs, and mobilized iron, leading to the formation of

massive magnetite bodies, iron oxide veins and iron-enriched itabirites. The second stage involved low-temperature and low- to medium-salinity fluids, resulting in oxidation of magnetite to martite, and formation of anhedral and subhedral hematite (Fig. 2a). Granular hematite resulted from the recrystallization of these iron oxide types during metamorphism. The third mineralization stage involved percolation of saline hydrothermal fluids along shear zones, with the formation of tabular hematite, precipitated from low-temperature hydrothermal fluids. Specularite (Fig. 2b) subsequently formed along shear zones under high-strain and high-temperature conditions, overgrowing previous granular hematite. The Neoproterozoic, Brasiliano tectonic event was characterized by intense deformation in the eastern domain of the QF, where iron ores display a schistose structure, with well developed specularite crystals formed at high temperatures. These ores may have been formed under lower crustal conditions during the peak of the Rhyacian-aged orogeny, and then were thrust upwards to shallower levels during the Brasiliano Orogeny (Rosière et al. 2008).

3.2 Corumbá

Located near the Brazilian-Bolivian border (south of the town of Corumbá), the Urucum deposit lies between the southeastern edge of the Amazon craton and the northeastern corner of the Rio Apa block (Fig. 1 of Angerer et al. 2016).

The Banda Alta Formation of the Neoproterozoic Jacadigo Group in the Urucum massif, southwestern Brazil, represents one of the largest known Neoproterozoic hematite iron formations
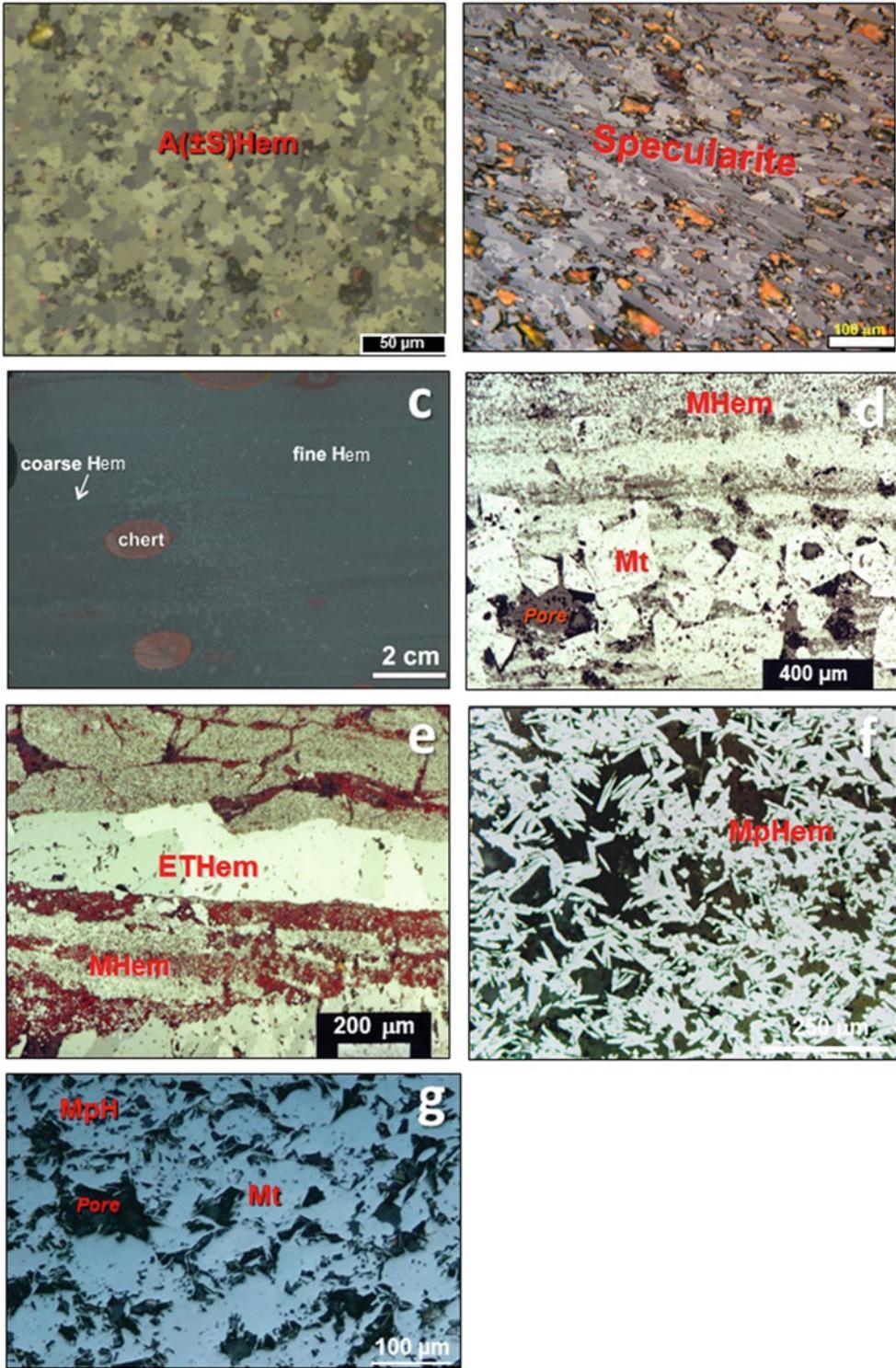
(Fig. 1b). They are nodular and laminated, as well as banded, and are hereafter referred to as BIF following Walde and Hagemann (2007) and Angerer et al. (2016, and references therein). Several manganese oxide layers in the lower stratigraphic zone, as well as colluvial hematite ore (∼45 to 62 wt% Fe) near the land surface, represent significant metal resources (Walde et al. 1981; Urban et al. 1992; Walde and Hagemann 2007). In the Urucum massif, the lowermost siliciclastic units of the Urucum Formation, the intermediate Córrego das Pedras Formation, and/or upper BIF and diamictite layers of the Banda Alta Formation, rest unconformably above a gneissic basement high of the Rio Apa Block (Dorr 1945). The depositional age is uncertain, and bracketed by a K–Ar cooling age of basement granites at 889 ± 44 Ma (Hasui and Almeida 1970) and an Ar–Ar age of diagenetic cryptomelane in the Mn-formation at 587 ± 7 Ma (Piacentini et al. 2013).

The banded and chemical-sedimentary nature of most of the hematite-rich rocks in the Banda Alta Formation has been established by several stratigraphic, petrographic and geochemical studies (Urban et al. 1992; Klein and Ladeira 2004; Freitas et al. 2011; Angerer et al. 2016; Viehmann et al. 2016). Stratigraphic studies have established a variable BIF stratigraphy across the Urucum region (Urban et al. 1992), with dolomite-rich BIF facies in the lower stratigraphic zone of the southeastern part of the massif (Angerer et al. 2016). A glaciomarine depositional environment has been invoked as a suitable setting for Neoproterozoic iron formations, and several examples are been correlated with Neoproterozoic ice ages (see reviews by Hoffman et al. 2011; Gaucher et al. 2015; Cox et al. 2013, 2016). According to Angerer et al. (2016), the Banda Alta Formation BIF was deposited in a redox-stratified marine sub-basin, which was strongly influenced by glacial advance/ retreat cycles with temporary influx of continental freshwater and upwelling seawater from deeper anoxic parts. Rare earth elements, base metal ratios, and ε_{Nd} suggest that dissolved metals in the Urucum seawater were most likely derived from a mix of terrigenous material of the nearby Neoproterozoic Brasília Belt (Viehmann et al. 2016) and low-temperature, hydrothermal fluids (Angerer et al. 2016). No evidence exists for high-temperature fluid source (Viehmann et al. 2016).

The supergene upgrade of the Corumbá hematite-rich BIF includes various significant processes that have led to the sought-after, colluvial high-grade iron ore (Walde and Hagemann 2007). The congruent dissolution of chert and carbonate from BIF forms the prominent, cavernous high-grade ore in the colluvium. The dissolution of dolomite from the upper carbonate-rich facies was probably the most efficient upgrade process, which is indicated by the absence of carbonate, but abundance of chert in BIF near the surface. Incongruent chert and dolomite dissolution, under the influence of Fe-rich weathering solutions, leaving fine, ochreous goethite residuals between partially dissolved hematite layers, was the second-most important process.

3.3 Carajás, Serra Norte Jaspilite-Hosted High-Grade Iron Ore Deposits

The Carajás mineral province, located in the eastern part of the state of Pará, Brazil, is the best-known, preserved Archean region of the Amazon Craton (Fig. 1 of Figueiredo e Silva et al. 2013). It is considered one of most important mineral provinces of the world, with regards to production and growing potential for Fe, Mn, Cu, Au, Ni, U, Ag, Pd, Pt, Os, Zn and W. The Carajás iron ore deposits (Fig. 1c) were discovered in 1967, with reserves estimated at 17 Gt of iron ore (> 64% Fe). The so-called Serra Norte iron deposits are hosted by the Archean metavolcanic-sedimentary sequence of the Grão Pará Group, Itacaiúnas Supergroup (DOCEGEO 1988). The protoliths to iron mineralization are jaspilites, under- and overlain by greenschist-facies metabasalts. The basal contact of high-grade iron ore is defined by a hydrothermally altered basaltic rock mainly composed of chlorite and microplaty hematite. The major Serra Norte N1, N4E, N4W, N5E and N5S iron ore deposits

are distributed along, and structurally controlled by, the northern flank of the Carajás fold (Rosière et al. 2006).

Practically unmetamorphosed, Archean BIF (jaspilite) hosts high-grade iron ore (64% Fe) that is mainly composed of martite, and different types of hematite (Figueiredo e Silva et al. 2008, 2013). Three hydrothermal alteration zones are associated with the Serra Norte deposits: (1) A distal zone, which formed early (e.g., N4 deposit), is mainly characterized by recrystallization of jasper and removal of the original, fine-grained iron oxides, and by formation of euhedral to anhedral magnetite. This magnetite formed: (i) overgrowths on microcrystalline hematite (Fig. 2d; MHem) in jasper layers, (ii) grains in the nuclei of recrystallized chert, uniformly associated with crosscutting quartz veins, or (iii) grains in equilibrium with vein quartz and calcite. (2) An intermediate zone is characterized by widespread martitization (Fig. 2d), with common quartz-hematite veins that contain microplaty hematite and subordinate sulfides (e.g., N5S deposit). Precipitation of microplaty hematite and extensive martite alteration followed the formation of magnetite in the early alteration stage. (3) A proximal zone that was produced by later alteration events and was synchronous with the main ore-forming event. This zone represents the most advanced stage of hydrothermal alteration. It contains the high-grade iron ore, with varying types of hard and hard-porous ores. A complete oxide sequence defined by martite $\rightarrow$ microplaty hematite $\rightarrow$ anhedral hematite $\rightarrow$ euhedral-tabular hematite (Fig. 2e) is best documented in the N5E deposit, which contains the largest volume of hard, high-grade iron ore in Carajás (see also Lobato et al. 2008).

A dual magmatic-meteoric hydrothermal fluid-flow model is proposed for the high-grade iron ore (Figueiredo e Silva et. al. 2013; Hagemann et al. 2016), in which an early, saline, ascending modified magmatic fluid caused widespread oxidation of magnetite to hematite. Progressive influx of light ^{18}O meteoric water, mixing with the ascending magmatic fluids, is interpreted to have been initiated during the intermediate stage of alteration. The advanced and final hydrothermal stage was dominated by massive influx of low salinity, meteoric water, which maintained intermediate temperatures of 240–310 °C, and concomitant formation of the paragenetically latest, tabular hematite (Fig. 2e).

The giant Carajás iron deposits are unique in their setting within an Archean granite-greenstone belt and their modified magmatic-meteoric hydrothermal system, when compared to the other two end-member BIF iron deposit types, namely the basin-related Hamersley type and the metamorphosed metasedimentary, basin-related Quadrilátero-Ferrífero type (e.g., Hagemann et al. 2016).

The Carajás BIF iron ore system also constitutes a somewhat special case in that although the protolith jaspilite is Archean in age (Santos 2003), the upgrade of BIF to high-grade iron ore took place during Paleoproterozoic times (Figueiredo e Silva et al. 2008; Santos et al. 2010).

3.4 Hamersley High-Grade Iron Ore Deposits

The Hamersley province covers an area of about 80,000 km^2, and is situated between Archean basement complexes of the Yilgarn and Pilbara cratons (Fig. 1d). The stratigraphy in the province constitutes mostly Neo-Archean–Paleoproterozoic (2800–2300 Ma) sedimentary rocks of the Mount Bruce Supergroup resting on the Pilbara craton. The BIFs of the Hamersley Group are part of the Mount Bruce Supergroup, and host numerous bedded, high-grade orebodies within the ∼2.6 Ga Marra Mamba Iron Formation (IF) and the ∼2.5 Ga Brockman IF (for reviews see Thorne et al. 2008; Angerer et al. 2014, and references therein). The main types of BIF-hosted high-grade iron ores, presently produced from the Hamersley province, are martite-microplaty (Fig. 2f) hematite ore, hosted in the Brockman IF, and martite-goethite ore in the Brockman and Marra Mamba IFs.

The regionally abundant least-altered, yet low-grade metamorphosed BIF, show variably layered quartz-magnetite $\pm$ "early" hematite $\pm$

Fe-silicate $\pm$ Fe-carbonate assemblage (Krapež et al. 2003; Klein 2005). Martite-microplaty (Fig. 2f and g) hematite ore consists almost entirely of martite bands or aggregates set in a porous (up to 30 vol. %), randomly orientated network of fine-grained (10–500 μm) hematite. In high-grade ore zones, BIF and locally associated shales are completely hematitized or leached leaving a martite residue. In peripheral zones, these rocks are hydrothermally altered, displaying distal carbonate–silicate-magnetite, intermediate carbonate–silicate-hematite, and proximal medium-grade martite-microplaty hematite associations (Thorne et al. 2008). The major martite-microplaty hematite orebodies include Mount Whaleback, Mount Tom Price, Paraburdoo, and Channar, with satellite deposits such as OB25 at Eastern Ridge and Hashimoto, both located in the South Ophthalmia Range (Thorne et al. 2008). The hematite orebodies are dominantly controlled by normal fault systems, i.e., the Southern Batter Fault in Mount Tom Price, the 4East Fault system in Paraburdoo, and the Central Fault and East Footwall Fault Zones in Mount Whaleback (Dalstra and Rosière 2008). Orebodies commonly extend below the weathering front to great depths, in places down to 500 m (e.g., Mount Whaleback). Goethite is present above the weathering front.

Martite-goethite ore consists of martite and various amounts of vitreous and ochreous goethite, with only very local microplaty hematite (Clout 2005). Important martite-goethite ore deposits include the numerous Marra Mamba iron formation (IF) orebodies in the Mining Area C, Hope Downs, and Chichester Range areas, as well as the Brockman BIF deposits in the South Ophthalmia Range, Mining Area C (Packsaddle), and Marillana area. The South Ophthalmia Range, Mining Area C, and Hope Downs orebodies are located in the structurally complex flanks of regional folds. On the other hand, the Chichester Range and Marillana deposits are extensive areas of almost flat-lying mineralized BIF lacking any structural complexity (Clout 2005). Generally, martite-goethite ore is limited to (paleo-) weathering zones and rarely reach deeper than 150 m.

The origin of the high-grade iron ore of the Hamersley province is subject to debate. Early work established the importance of supergene quartz leaching and goethite replacement in the upgrading of BIF to martite-goethite ore (Morris et al. 1980; Morris 1983; Morris and Horwitz 1983). Lascelles (2006) advocates a supergene-modified syngenetic model, whereas a supergene-metamorphic model was invoked by others (Morris and Fletcher 1987; Morris 1985, 2002) to explain the development of microplaty hematite-rich orebodies. Supergene-modified, hypogene fluid models, involving hot fluids and complex alteration, are suggested by various other researchers (Barley et al. 1999; Hagemann et al. 1999; Powell et al. 1999; Taylor et al. 2001; Webb et al. 2004).

4 Methods

Carajás and Hamersley samples were analyzed for Fe isotopes at the Geotop Isotope Laboratory, Université du Québec à Montréal, according to the methods used in Halverson et al. (2011). Approximately 30 mg of pulverized samples were weighed into Savillex™ teflon beaker and dissolved for 24 h at 80 °C in a mixture of double-distilled 6 M HCl, 7 M HNO_3, and 50% HF. The samples were then evaporated to dryness with excess HNO_3 to prevent the formation of apatite, then re-dissolved in 2.0 mL of concentrated aqua regia and dried down again. The samples were taken up again in 2.0 mL 2 M HCl and again dried down. The resulting salt was finally re-dissolved in 0.5 mL of 6 M HCl for ion exchange chromatography. Iron was separated using Bio Rad AG1 X4 (200–400 mesh) resin loaded into custom Teflon columns and separated from the matrix using 6 M HCl. Purified iron was eluted from the columns in 2 M HCl, which was then dried down and subsequently taken up in 0.5 M HNO_3 and diluted for isotopic measurement. Solutions were analyzed at the Geotop Isotope Laboratory at the Université du Québec à Montréal on a Nu Plasma II multi-collector inductively coupled plasma mass spectrometer (MC-ICP-MS) in

high-resolution mode via wet sample introduction. Instrumental mass bias was corrected by using standard-sample-standard bracketing. Each sample was analyzed three times yielding typical 1-sigma errors of < 0.1 per mil for δ^{57}Fe and < 0.05 per mil for δ^{56}Fe. The data are reported in standard delta notation relative to the IRMM-14 reference standard.

Oxygen isotopes of samples from the Hamersley province and from Corumbá were analyzed at the Scottish Universities Environmental Research Centre (SUERC), University of Glasgow. Oxide separates were analyzed using a laser fluorination procedure, involving total sample reaction with excess ClF_3 using a CO_2 laser as a heat source (in excess of 1500 °C; following Sharp 1990). All combustions resulted in 100% release of O_2 from the silica lattice. This O_2 was then converted to CO_2 by reaction with hot graphite, then analyzed on-line by a VG Optima spectrometer. Reproducibility was within ± 0.2‰ (1σ), based on reproducibility of one international and two internal laboratory standards: UWG 2 (garnet = 5.8‰), GP147 (feldspar = 7.2‰) and SES 1 (quartz = 10.2‰). All results are reported in standard notation (δ^{18}O) as per mil (‰) deviations from the Standard Mean Ocean Water (V-SMOW) standard.

5 Published Iron and Oxygen Isotope Datasets

5.1 Quadrilátero Ferrífero (QF)

A series of deposits (Fig. 1a) located in different deformational domains of the QF have available iron isotope data (Table 1). These were obtained for both iron ores and their host itabirites and show significant variations (Mendes et al. 2017).

The QF itabirites display two groups (Fig. 3): quartz itabirites, which plot in two clusters, and carbonate itabirites that coincide with the lowest iron isotope cluster of the quartz itabirites. The δ^{56}Fe values of itabirites have very similar iron isotope ratios, varying from –0.95 to 0.27‰ (mean = –0.25‰; n = 14). The ranges for the

different studied mines are: Usiminas (δ^{56}Fe from 0.02 ± 0.02‰ to 0.27 ± 0.07‰); Pau Branco (δ^{56}Fe from -0.09 ± 0.21 and 0.11 ± 0.09‰); Várzea do Lopes (δ^{56}Fe = -0.65 ± 0.04‰); Casa de Pedra (δ^{56}Fe = -0.95 ± 0.11 to -0.84 ± 0.08‰). Itabirites from Várzea do Lopes and Casa de Pedra have significantly lighter δ^{56}Fe values. Quartz itabirites from the eastern domain resulted in δ^{56}Fe varying from -0.12 ± 0.01 to 0.11 ± 0.03‰ (Conceição Mine and Morro do Agudo, respectively).

The deposition of the precursor sedimentary rocks to the QF itabirites was probably favored by the presence of an oasis of free oxygen in the Minas basin. The negative to low, near-zero positive δ^{56}Fe values for most of the quartz itabirites lie close or within the range reported for hydrothermal fluids (δ^{56}Fe ≈ –0.50 to 0‰), suggesting complete or near-complete oxidation of the dissolved Fe(II), which seems to be an emerging scenario for Paleoproterozoic BIFs (Planavsky et al. 2012). The most depleted δ^{56}Fe values (–0.95 to –0.65‰) of quartz itabirites may be explained by Rayleigh-type fractionation and BIF deposition further away from the hydrothermal source. Similarly, δ^{56}Fe values for carbonate and amphibole itabirites, deposited in shallower settings, were also a result of precipitation from a depleted source away from hydrothermal vents with negligible riverine Fe (Mendes et al. 2017).

Even though some inferences of positioning to the iron source can be made by the isotope signature of Cauê BIFs, it is not straightforward to define a stratigraphic sequencing, or the relative position on the depositional basin for the BIFs based on isotope data for the studied iron deposits, as a result of successive deformational events and stratigraphic inversions. Also, there is no record of a possible hydrothermal source for the iron deposited in the Minas Basin, making it impossible to determine the relative distance from the submarine volcanic centers. Nevertheless, the iron isotope values suggest that the Usiminas and Pau Branco deposits, and deposits from the eastern domains were probably located relatively closer to the iron sources than the Várzea do Lopes and Casa de Pedra deposits

Table 1 Sample/mineral list and isotope (iron and oxygen) composition of rock and mineral specimens from the Brazilian Quadrilátero Ferrífero (QF), Corumbá, and Carajás iron districts, as well as from the Hamersley province in Australia

Region	Classification	Sample type	Deposit	δ^{56}Fe (‰)	σ	δ^{57}Fe (‰)	σ	δ^{18}O (‰)	Total Fe$_2$O$_3$ (%)	Reference
QF	Quartz itabirite	Martite-mag-hem and qtz layers	Usiminas	0.08	0.03	0.11	0.04	–	50.9	Mendes et al. (2017)
QF	Quartz itabirite	Martite-mag-hem and qtz layers	Usiminas	0.27	0.07	0.35	0.21	–	57.2	Mendes et al. (2017)
QF	Quartz itabirite	Martite-mag-hem and qtz layers	Usiminas	0.02	0.02	– 0.07	0.14	–	66.3	Mendes et al. (2017)
QF	Massive iron ore	Anhedral hem and martite relicts	Usiminas	– 0.34	0.08	– 0.56	0.12	–	99.2	Mendes et al. (2017)
QF	Quartz itabirite	Martite-goethite-mag and qtz layers	Usiminas	0.16	0.04	0.19	0.07	–	47.2	Mendes et al. (2017)
QF	Massive iron ore	Anhedral granular mag	Bocaina	– 0.45	0.08	– 0.83	0.27	–	–	Mendes et al. (2017)
QF	Dolomitic itabirite	Dolomite and mag layers	Bocaina	– 0.61	0.13	– 0.93	0.11	–	–	Mendes et al. (2017)
QF	Specularite	Specular hem	Pau Branco	– 0.75	0.07	– 1.25	0.11	–	–	Mendes et al. (2017)
QF	Banded iron ore	Lamellar and granular hem	Pau Branco	– 0.22	0.04	– 0.33	0.09	–	–	Mendes et al. (2017)
QF	Specularite	Specular hem	Pau Branco	– 0.08	0.04	– 0.26	0.10	–	–	Mendes et al. (2017)
QF	Quartz itabirite	Martite-goethite-mag and qtz layers	Pau Branco	– 0.09	0.21	– 0.15	0.31	–	83.2	Mendes et al. (2017)
QF	Quartz itabirite	Martite-goethite and qtz layers	Pau Branco	0.11	0.09	0.13	0.15	–	40.3	Mendes et al. (2017)
QF	Massive iron ore	Anhedral-granular-lamellar hem	Pau Branco	– 0.26	0.00	– 0.45	0.10	–	99.1	Mendes et al. (2017)
QF	Banded iron ore	Lamellar-anhedral-granular hem and martite layers	Pau Branco	0.29	0.04	0.38	0.03	–	98.4	Mendes et al. (2017)
QF	Massive iron ore	Martite-granular-lamellar hem	Várzea do Lopes	– 0.69	0.03	– 0.99	0.06	–	–	Mendes et al. (2017)
QF	Schistose iron ore	Lamellar-granular-anhedral hem	Várzea do Lopes	– 0.42	0.12	– 0.66	0.18	–	–	Mendes et al. (2017)

(continued)

Table 1 (continued)

Region	Classification	Sample type	Deposit	δ56Fe (‰)	σ	δ57Fe (‰)	σ	δ18O (‰)	Total Fe2O3 (%)	Reference
QF	Specularite	Specular hem	Várzea do Lopes	− 0.31	0.02	− 0.45	0.29	–	–	Mendes et al. (2017)
QF	Quartz itabirite	Martite-granular hem-goethite and qtz layers	Várzea do Lopes	− 0.65	0.04	− 0.99	0.08	–	75.2	Mendes et al. (2017)
QF	Specularite	Specular hem	Várzea do Lopes	0.83	0.38	1.29	0.58	–	–	Mendes et al. (2017)
QF	Quartz itabirite	Martite-hem-mag and qtz layers	Casa de Pedra	− 0.84	0.08	− 1.27	0.12	–	52.8	Mendes et al. (2017)
QF	Amphibolitic itabirite	Magnetitic and amphibole-carbonate layers	Casa de Pedra	− 0.95	0.09	− 1.45	0.14	–	–	Mendes et al. (2017)
QF	Brecciated/banded iron ore	Banded/brecciated martite-hem-mag	Casa de Pedra	− 0.51	0.04	− 0.79	0.06	–	98.5	Mendes et al. (2017)
QF	Specularite	Specular hem	Casa de Pedra	− 0.62	0.09	− 0.91	0.18	–	96.2	Mendes et al. (2017)
QF	Brecciated iron ore	Brecciated martite-mag-hem in goethite matrix	Casa de Pedra	− 0.31	0.02	− 0.45	0.29	–	–	Mendes et al. (2017)
QF	Brecciated iron ore	Martite-mag-hem in goethite matrix	Casa de Pedra	− 0.13	0.06	− 0.13	0.08	–	–	Mendes et al. (2017)
QF	Massive iron ore	Martite	Casa de Pedra	− 0.71	0.05	− 1.10	0.13	–	–	Mendes et al. (2017)
QF	Massive iron ore	Martite-mag-granular hem	Casa de Pedra	− 0.80	0.01	− 1.15	0.03	–	96.6	Mendes et al. (2017)
QF	Quartz itabirite	Martite-mag and qtz layers	Casa de Pedra	− 0.95	0.11	− 1.49	0.12	–	–	Mendes et al. (2017)
QF	Schistose iron ore	Lamellar-specular hem	Morro do Agudo	0.37	0.06	0.57	0.20	–	–	Mendes et al. (2017)
QF	Quartz itabirite	Lamellar-specular hem and qtz layers	Morro do Agudo	0.11	0.03	0.25	0.11	–	–	Mendes et al. (2017)
QF	Schistose iron ore	Lamellar-specular hematite	Alegria	− 0.09	0.08	− 0.13	0.14	–	–	Mendes et al. (2017)
QF	Schistose iron ore	Lamellar-specular hematite	Andrade	0.27	0.01	0.43	0.02	–	–	Mendes et al. (2017)

(continued)

Table 1 (continued)

Region	Classification	Sample type	Deposit	$\delta^{56}Fe$ (‰)	σ	$\delta^{57}Fe$ (‰)	σ	$\delta^{18}O$ (‰)	Total Fe_2O_3 (%)	Reference
QF	Quartz itabirite	Lamellar-specular hematite and qtz layers	Conceição	− 0.12	0.01	− 0.15	0.06	–	–	Mendes et al. (2017)
QF	Schistose iron ore	Lamellar-specular hematite	Conceição	0.04	0.08	0.04	0.23	–	–	Mendes et al. (2017)
QF	Quartz itabirite	Lamellar-specular hematite and qtz layers	Cauê	− 0.02	0.14	− 0.06	0.21	–	–	Mendes et al. (2017)
Corumbá	Reworked hem mud	Hematite	Santa Cruz	0.01	0.08	− 0.04	0.07	− 2.4	94.7	Angerer et al. (2016)
Corumbá	Reworked hem mud	Hematite	Santa Cruz	− 0.18	0.01	− 0.25	0.01	− 2.4	94.7	Angerer et al. (2016)
Corumbá	Chert-hem BIF	Hematite	Santa Cruz	− 0.49	0.06	− 0.71	0.07	4.6	65.3	Angerer et al. (2016)
Corumbá	Chert-dolomite-hem BIF	Hematite	Santa Cruz	− 0.83	0.02	− 1.22	0.04	3.4	62.7	Angerer et al. (2016)
Corumbá	Dolomite-chert-hem BIF	Hematite	Santa Cruz	− 1.83	0.02	− 2.62	0.03	1.3	62.1	Angerer et al. (2016)
Carajás	Jaspilite	Hem (iron-rich microband)	N4	1.13	0.17	1.67	0.23	–	94.7	Fabre et al. (2011)
Carajás	Jaspilite	Hem (iron-rich microband)	N4	1.07	0.04	1.61	0.06	–	89.6	Fabre et al. (2011)
Carajás	Jaspilite	Hem (iron-rich microband)	N4	1.16	0.12	1.74	0.12	–	94.2	Fabre et al. (2011)
Carajás	Jaspilite	Hem-goe (silica-rich microband)	N4	1.46	0.04	2.18	0.08	–	47.2	Fabre et al. (2011)
Carajás	Jaspilite	Hem-goe (iron-rich microband[2])	N4	1.41	0.08	2.07	0.01	–	19.0	Fabre et al. (2011)
Carajás	Jaspilite[1]	Hem-Goe (iron-rich microband)	N4	1.5	0.06	2.26	0.02	–	62.6	Fabre et al. (2011)
Carajás	Jaspilite	Hematite (silica-rich microband)	N4	1.75	0.04	2.58	0.21	–	32.0	Fabre et al. (2011)
Carajás	Jaspilite	Hematite (iron-rich microband)	N4	1.41	0.11	2.09	0.12	–	50.6	Fabre et al. (2011)
Carajás	Jaspilite	Hem-Mag (iron-rich microband)	N4	1.56	0.09	2.30	0.14	–	64.9	Fabre et al. (2011)
Carajás	High-grade ore	Anhedral hem	N5E	1.08	0.02	1.60	0.03	− 6.9	–	This study
Carajás	High-grade ore	Anhedral hem	N5E	0.74	0.04	0.69	0.01	−8.5	–	This study
Carajás	High-grade ore	Anhedral hem	N5E	0.51	0.01	0.74	0.11	−6.2	67.84	This study
Carajás	Jaspilite	Jaspilite	N4E	1.76	0.02	2.64	0.04	–	–	This study

(continued)

Table 1 (continued)

Region	Classification	Sample type	Deposit	δ56Fe (‰)	σ	δ57Fe (‰)	σ	δ18O (‰)	σ	Total Fe2O3 (%)	Reference
Carajás	Jaspilite	Jaspilite	N5S	0.64	0.01	0.92	0.01	10.7	0.01	–	This study
Carajás	Jaspilite	Magnetite	N5S	0.74	0.04	1.13	0.07	–	–	–	This study
Carajás	Jaspilite	Magnetite	N4W	0.95	0.01	1.37	0.03	3.8	–	–	This study
Carajás	Hydrothermally altered jaspilite	Magnetite (veins)	N4E	1.10	0.06	1.65	0.09	–0.4	–	–	This study
Carajás	Hydrothermally altered jaspilite	Magnetite (veins)	N4E	1.24	0.01	1.83	0.03	–0.1	–	–	This study
Carajás	High-grade ore	Martite	N4E	1.16	0.00	1.69	0.02	–4.3	–	61.95	This study
Carajás	High-grade ore	Martite	N5E	0.69	0.06	0.99	0.10	–5.9	–	96.51	This study
Carajás	High-grade ore	Martite (±MpHem-THem)	N5E	0.53	0.02	0.75	0.01	–	–	–	This study
Carajás	High-grade ore	Martite (±MpHem-THem)	N5E	0.62	0.01	0.92	0.01	–6.6	–	–	This study
Carajás	High-grade ore	Microplaty hem	N4E	0.67	0.02	0.97	0.02	–5.5	–	82.09	This study
Carajás	High-grade ore	Microplaty hem	N5E	0.62	0.01	0.93	0.02	–5.8	–	–	This study
Carajás	High-grade ore	Microplaty hem	N5S	0.46	0.01	0.69	0.01	–2.7	–	–	This study
Carajás	High-grade ore	Microplaty hem (±AHem)	N5S	1.11	0.02	1.63	0.00	–2.4	–	–	This study
Carajás	High-grade ore	Tabular hem	N5E	–0.30	–	–	–	–7.2	–	65.55	This study
Hamersley	Mt Newman BIF	Magnetite prox	Mesa Gap	0.19	0.02	0.28	0.03	3.29	–	53.87	This study
Hamersley	Dales Gorge BIF	Magnetite prox	Eastern Ridge	–0.30	0.00	–0.39	0.00	3.10	–	48.36	This study
Hamersley	Siderite breccia	Siderite	Marillana	–1.24	0.01	–1.84	0.02	26.34	–	57.40	This study
Hamersley	Siderite breccia	Siderite	Marillana	–0.57	0.05	–0.81	0.10	26.54	–	57.40	This study
Hamersley	Martite-Hem ore	MpHem-martite	Hashimoto	0.27	0.01	0.46	0.03	–7.47	–	96.71	This study
Hamersley	Martite-Hem ore	MpHem-martite	Whaleback	–0.29	0.01	–0.40	0.01	–7.57	–	98.30	This study
Hamersley	Martite-Hem ore	MpHem-martite	Whaleback	0.37	0.03	0.58	0.06	–0.63	–	97.92	This study
Hamersley	Martite-Hem ore-Goe-ore	MpHem-martite	Paraburdoo	–0.10	0.03	–0.14	0.05	–5.90	–	95.12	This study
Hamersley	Martite-Hem ore	MpHem-martite	Paraburdoo	0.35	0.02	0.53	0.04	–5.80	–	95.12	This study
Hamersley	Tc-carb BIF	MpHem-martite	Tom Price	0.05	0.03	0.10	0.05	–9.00	–	97.87	This study
Hamersley	Martite-Hem ore	MpHem-martite	Tom Price	–0.16	0.01	–0.25	0.03	–5.50	–	97.87	This study

(continued)

Table 1 (continued)

Region	Classification	Sample type	Deposit	δ56Fe (‰)	σ	δ57Fe (‰)	σ	δ18O (‰)	Total Fe2O3 (%)	Reference
Hamersley	Martite-Hem ore	MpHem-martite	Tom Price	1.02	0.10	1.60	0.10	− 5.10	97.87	This study
Hamersley	Martite-Hem ore	MpHem-martite	Tom Price	0.58	0.02	0.92	0.05	− 2.90	97.87	This study
Hamersley	Martite-Hem ore	MpHem-martite	Channar	0.22	0.01	0.32	0.04	n.a	–	This study
Hamersley	Dales Gorge BIF	Martite	Tom Price	1.09	0.01	1.61	0.02	n.a	–	This study
Hamersley	Dales Gorge BIF	Martite	Tom Price	1.00	0.02	1.45	0.08	8.80	–	This study
Hamersley	Martite ore	Martite	Packsaddle	0.81	0.02	1.18	0.04	n.a	44.13	This study
Hamersley	Martite ore	Martite	Marillana	0.78	0.02	1.16	0.03	− 3.12	86.57	This study
Hamersley	Dales Gorge BIF	Hematite	Paraburdoo	− 0.82 (− 0.9 to − 0.76)	0.05	–	–	–	–	Steinhoefel et al. (2010)
Hamersley	Dales Gorge BIF	Magnetite	Paraburdoo	− 0.87 (−0.94 to − 0.82)	0.06	–	–	–	–	Steinhoefel et al. (2010)
Hamersley	Dales Gorge BIF	Siderite	Paraburdoo	− 2.08 (− 2.18 to − 1.97)	0.15	–	–	–	–	Steinhoefel et al. (2010)
Hamersley	Dales Gorge BIF	Magnetite	Paraburdoo	− 0.01 (− 1.21 to 1.19)	0.49	–	–	–	–	Johnson et al. (2008a)
Hamersley	Dales Gorge BIF	Siderite	Paraburdoo	− 0.76 (− 2.06 to 1.00)	0.59	–	–	–	–	Johnson et al. (2008a)
Hamersley	Dales Gorge BIF	Magnetite	Wittenoom Gorge	0.37 (− 0.29 to 1.19)	0.38	–	–	–	–	Craddock & Dauphas (2011)
Hamersley	Dales Gorge BIF	Magnetite	Wittenoom Gorge	− 0.07	0.49	–	–	–	–	Craddock & Dauphas (2011)
Hamersley	Dales Gorge BIF	Siderite-min	Wittenoom Gorge	− 1.08	–	–	–	–	–	Craddock & Dauphas (2011)
Hamersley	Dales Gorge BIF	Siderite-max	Wittenoom Gorge	0.79	–	–	–	–	–	Craddock & Dauphas (2011)
Hamersley	Dales Gorge BIF	Magnetite	Yampire Gorge	0.51 (− 0.16 to 1.04)	0.35	–	–	–	–	Craddock & Dauphas (2011)
Hamersley	Dales Gorge BIF	Siderite	Yampire Gorge	0.22 (− 0.40 to 1.21)	0.45	–	–	6.8	–	Craddock & Dauphas (2011)

Abbreviations: AHem = anhedral hematite; amph = amphibole; avg = average; Goe = goethite; Hem = hematite; Mag = magnetite; max = maximum; min = minimum; MpHem = microplaty hematite; n.a. = not analyzed; Quartz = qtz; Tc = talc; THem = tabular hematite.
[1]: classification according to this study; [2]: despite considered "iron-rich" by Fabre et al. (2011), it is relatively poor in iron.
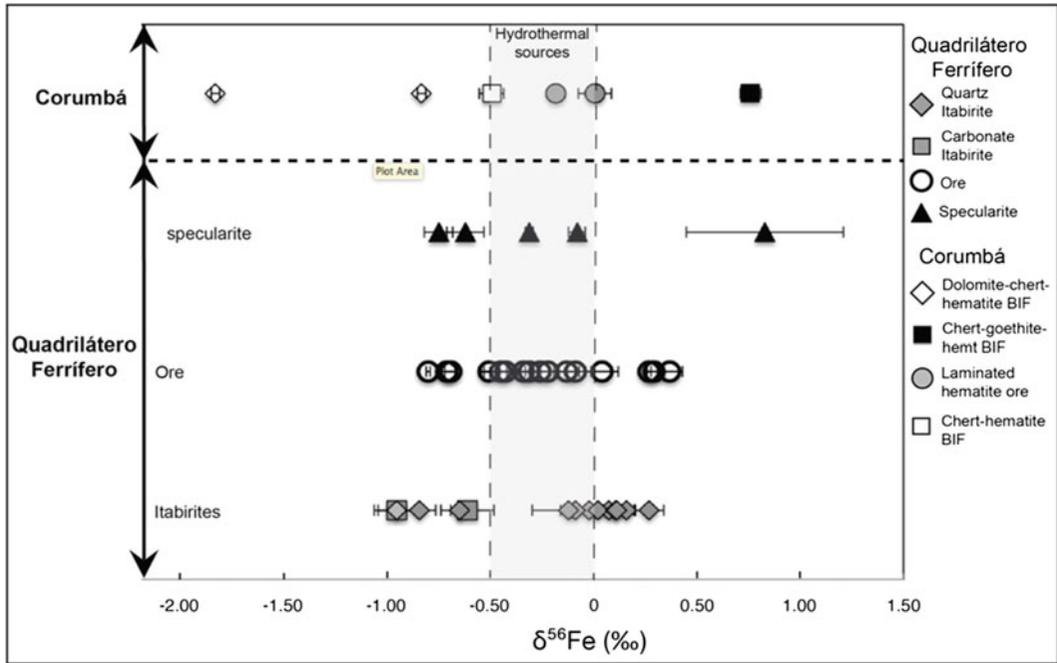
Fig. 3 Iron isotope data available for the Quadrilátero Ferrífero (Mendes et al. 2017) and Urucum (Corumbá) iron districts (Angerer et al. 2016), Brazil (Table 1). Field of hydrothermal source is $\delta^{56}Fe \approx -0.50$ to 0‰ (Beard et al. 2003; Severmann et al. 2004; Johnson et al. 2008b; Planavsky et al. 2012) is shown

(location in Fig. 1a). Casa de Pedra must have been deposited closer to the shallower platform, as suggested by the presence of carbonate.

The similarity between the iron isotope composition of iron ores and their host itabirites suggests that hydrothermal mineralization did not significantly alter the protore composition. Nevertheless, the isotopic compositions of iron ores from the low- and high-strain domains are quite different, and may reflect distinct conditions of hydrothermal mineralization as a result of variations in the thermodynamic conditions of the fluid, such as acidity, salinity and temperature (Rosière and Rios 2004; Rosière et al. 2008). Their conclusions are mainly based on the comparison of fluid inclusion data for each domain. Although no additional, new data are available, it is feasible to envisage redox variations to explain the indicated isotopic differences. Besides, mechanisms of iron isotope fractionation may vary within the same domain.

Some other data for the QF are available from Sampaio et al. (2018) and Teixeira et al. (2017). The former evaluated $\delta^{56}Fe$ signatures of magnetite-amphibole-carbonate-bearing itabirites, as well as their hydrothermal and weathering products. They investigated two drill holes in the Ouro Fino (OFS) and Gandarela (GS) synclines (Fig. 1a). The $\delta^{56}Fe$ ratios average -0.87‰ in the least altered samples. An analogous average of -0.84‰ was calculated for samples with goethite (after amphibole), and of -0.60‰ for those with martite, as well as in others with abundant goethite plus hematite (after martite). An average of $+0.41$‰ characterizes samples with martite plus abundant microplaty hematite and goethite, and minor clay minerals; a similar signature is calculated for samples just beneath the surface ground. The work of Teixeira et al. (2017) focused on itabirite samples from the Alegria Mine (Fig. 1a); they show $\delta^{56}Fe$ between $+0.51$ and $+1.33$‰.

5.1.1 Iron Isotope Data from Corumbá

The iron isotope data (Table 1) from Angerer et al. (2016) show negative values for BIF. They are low in the dolomite-rich hematite BIF (δ^{56}Fe − 1.83 and − 0.83‰; Fig. 3), and higher both in chert-hematite BIF (δ^{56}Fe − 0.49‰) and associated (high-grade) hematite mud (Fig. 2c; δ^{56}Fe = − 0.18 and 0.01‰). The goethite-altered BIF has positive values (δ^{56}Fe = 0.76‰). Variable iron isotope values in hematite are compatible with complex processes in the Fe source (Tsikos et al. 2010), during precipitation (Kunzmann et al. 2017), and during diagenesis (Johnson et al. 2008b). This dataset reflects several iron isotopic fractionation processes (Angerer et al. 2016) (see Discussion).

5.1.2 Iron Isotope Background at Carajás

The only available iron isotope data from the Serra Norte iron deposits in Carajás (Fabre et al. 2011; Table 1) resulted from the investigation of the redox changes of Earth's ocean and atmosphere between 2.7 and 2.1 Ga ago. Data were obtained from the protore BIF of the N4 (Fig. 1c) deposit and show consistent positive δ^{56}Fe values from + 1.75 to + 1.07‰, with a mean value of + 1.38 ± 0.23‰ (Table 1; Fig. 4). There is no significant difference in isotope signatures between iron oxides in silica (jasper)- and iron (microcrystalline hematite)-rich microbands (Table 1). According to Fabre et al. (2011), the values are among the most positive ever measured in BIF (Johnson et al. 2003, 2008a, b; Rouxel et al. 2005), except for older BIF like Akilia/Isua (Dauphas et al. 2004; Whitehouse and Fedo 2007; Thomazo et al. 2009). However, Planavsky et al. (2012) have shown that Archean BIF can also have negative δ^{56}Fe values. These authors obtained a δ^{56}Fe range from − 1.53 to + 1.61‰ for Archean to early Paleoproterozoic BIFs.

Partial oxidation of aqueous Fe(II) into Fe(III) near the ocean surface, subsequent to the upwelling of deep anoxic seawater, may have been responsible for the positive iron isotopic signatures (Fabre et al. 2011). According to these authors, the "extremely high" δ^{56}Fe values in the Carajás jaspilite resulted from oxidation of a high degree of the upwelling Fe(II) mass (i.e., 44%, based on assumed initial hydrothermal Fe with δ^{56}Fe of 0.0‰). Planavsky et al. (2012) indicate that positive δ^{56}Fe values for Archean BIFs are considered to result from non-quantitative iron oxidation in an oxygen-poor ocean, taking to the preferential deposition of the isotopically heavier iron.

Fig. 4 Results of Fe isotope composition of jaspilites and iron ore oxides (this study) from the Serra Norte iron district, Carajás, Brazil (Table 1). Published results by Fabre et al. (2011) are also shown
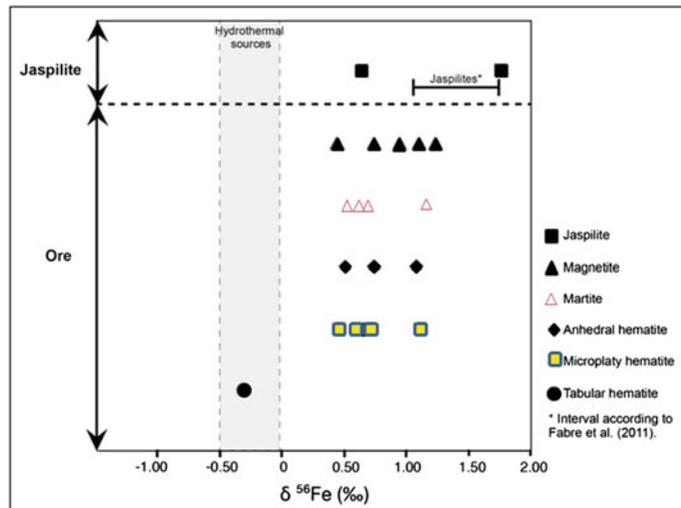
6 New Iron Isotope Results and Iron-Oxygen Isotope Pairing

6.1 Corumbá: Iron and Oxygen Isotope Pairing

Both iron and oxygen isotopes are sensitive indicators for low- to high-temperature fluid-rock interaction. The BIF and iron ore at Corumbá have a simple modal mineral composition, consisting of ~ 50–99 vol % hematite, with the remainder being chert and/or ferroan dolomite (Angerer et al. 2016). The relationship of oxygen and iron isotopes in hematite during BIF formation and subsequent alteration (hypogene and supergene hydrothermal) are investigated for this review.

Unpublished oxygen and published iron (Angerer et al. 2016) isotope data have been paired either using the same or lithologically and stratigraphically closely associated samples (Table 1). The oxygen isotope signature for Neoproterozoic seawater is unknown, but most probably between -8 and 0‰ (Jacobsen and

Kaufman 1999; Veizer et al. 1999). However, it is noted that the carbonate mean values reveal a long-term increase of about $+8$‰, in the Neoproterozoic and Cambrian to Present at 0‰ (Jacobsen and Kaufman 1999; Veizer et al. 1999). The $\delta^{18}O$ data reveal remarkable relationships with hematite $\delta^{56}Fe$ (Fig. 5). The chertdolomite-hematite BIF samples (C-6, C-11, C-14; Fig. 5) show $\delta^{18}O > 0$‰, and a negative correlation between $\delta^{18}O$ and $\delta^{56}Fe$. The range of data implies non-equilibrium conditions. The recrystallized (high-grade) hematite muds (H-14, H-15; Fig. 5) are significantly depleted in $\delta^{18}O$ (< 0‰), while showing non-fractionated $\delta^{56}Fe$ (± 0‰). Calculated $\delta^{18}O_{water}$ are up to 5‰ higher than that of $\delta^{18}O_{hematite}$. The large range of $\delta^{18}O_{water}$ results from uncertainties in the prevailing temperatures (see caption of Fig. 5 for temperature estimates and references of equations). Although there are no oxygen isotope data available for the goethite-altered BIF (H-17), a $\delta^{18}O$ value of < 0‰ may be assumed based on published data of world-wide supergene goethite-altered BIF (Gutzmer et al. 2006, and references

Fig. 5 Iron (Angerer et al. 2016) and oxygen (unpublished) isotope data for the Brazilian Urucum (Corumbá) iron district are shown in Table 1). Equilibrium temperatures 99 °C, 118 °C, 173 °C and $\delta^{18}O_{water}$ calculated with quartz-H_2O (Zheng 1993) and hematite-H_2O (Yapp 1990a,b) based on data from this study and from data of Hoefs et al. (1987)
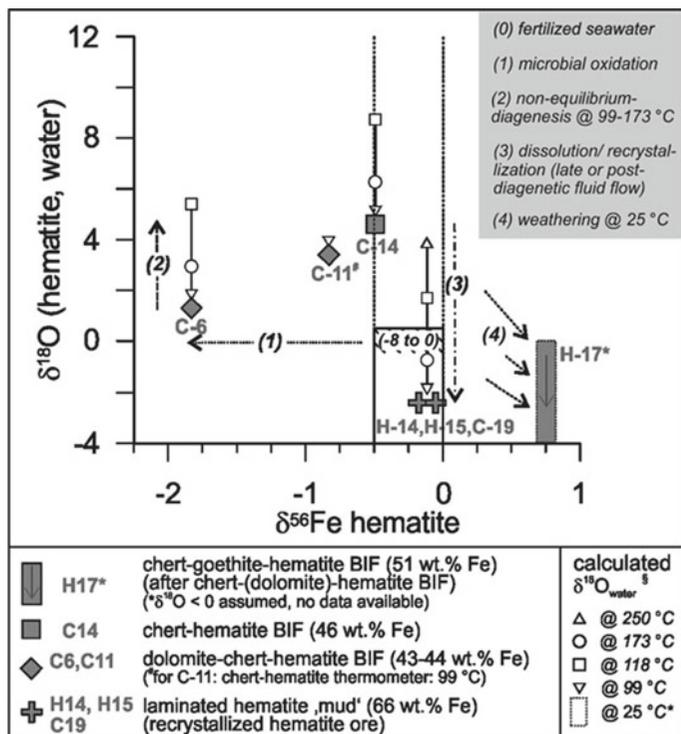
therein). The data pairing reveals that during certain alteration events, the isotope systems are coupled, while in others they are decoupled (see Discussion).

6.2 Carajás

Twenty samples of massive, high-grade iron ore samples from the Serra Norte N4 and N5 deposits were analyzed including separates of martite, microplaty hematite, anhedral hematite and tabular hematite (Figueiredo e Silva et al. 2013; Table 1). Signatures are positive and vary from + 0.44 to + 1.24‰, in δ^{56}Fe (Fig. 4). One sample has a negative δ^{56}Fe signature of –0.30‰, which corresponds to the late-stage tabular hematite (Fig. 2e).

Two jaspilite samples show δ^{56}Fe of + 1.76 and + 0.64‰ (Table 1), which are similar to results by Fabre et al. (2011). Other two samples correspond to hydrothermally altered jaspilites (Table 1), where magnetite occurs along quartz-carbonate veins; δ^{56}Fe values are + 1.10 and + 1.24‰.

Figure 4 shows a decrease in isotopic signature from Archean jaspilite (Fabre et al. 2011) to high-grade iron ore samples. There is also a slight trend towards negative values from earlier oxide magnetite to the latest tabular hematite (Fig. 2e), indicating some fractionation during advanced ore mineralization. Magnetite shows the most positive values (up to + 1.24‰); anhedral and microplaty hematite have the lowest values of δ^{56}Fe at + 0.51 and + 0.46‰, respectively.

6.2.1 Iron and Oxygen Isotope Pairing

Published oxygen isotope data (Figueiredo e Silva et al. 2013) have been paired with the present unpublished iron isotope data (Fig. 6a). Oxygen isotope analyses on different oxide species reveal that the heaviest $\delta^{18}O_{SMOW}$ value of + 10.7‰ is recorded for the protore jaspilite, followed by magnetite, between –0.4 to 3.8‰, and then by different hematite species such as microplaty, anhedral and tabular (Fig. 2e), which fall in the range of –8.5 to –2.4‰. Figure 6a

shows a progressive depletion in δ^{18}O values and δ^{56}Fe from the earliest hydrothermal oxide magnetite towards the latest tabular hematite.

6.3 Hamersley

Present iron isotope data from the Hamersley province derive from published data of the least-altered Dales Gorge Member BIF (Fig. 7), and from unpublished data of seventeen samples of altered BIF and hematite iron ore. The least-altered BIF samples come from the greater Paraburdoo region in the south (Johnson et al. 2008a; Steinhoefel et al. 2010), as well as from the Wittenoom Gorge and Yampire Gorge in the north of the province (Craddock and Dauphas 2011).

For the Dales Gorge Member, by far the most important host rock in the Brockman IF, samples include nine of hydrothermal martite-microplaty hematite iron ore; two of supergene martite ore; two of oxidized BIF; two of hydrothermally altered BIF; and two of early-siderite breccias. All rock samples were taken from diamond drill cores in various iron ore deposits (Table 1).

In BIF from the Paraburdoo-region, magnetite δ^{56}Fe values range from − 1.21 to + 1.19‰, (average − 0.01‰). Wittenoom Gorge magnetite BIF has δ^{56}Fe from − 0.29 to + 1.19‰ (average 0.37‰), and the Yampire Gorge from − 0.16 to + 1.04‰ (average 0.51‰). Taking only the interquartile ranges of each data subset into account, the entire BIF data range from − 0.3 to + 0.9‰ (Fig. 7). Associated anhedral hematite has slightly higher values (Table 1; Fig. 7).

Hematite in martite-microplaty hematite ore shows δ^{56}Fe values ranging from − 0.29 to + 1.02‰ (average 0.25‰). Magnetite in hydrothermally altered BIF, associated with the ore, shows δ^{56}Fe values ranging from − 0.30 to + 0.05‰. Martite from both oxidized BIF and iron ore shows distinctively heavier ^{56}Fe isotopes (+ 0.80 to + 1.10‰) compared with least-altered BIF and microplaty hematite ore (Fig. 7). A limiting factor prohibiting the exact measurement of isotope fractionation related to iron ore formation is the absence of a true precursor BIF sample for

Fig. 6 Calculated δ^{56}Fe versus δ^{18}O for: **a** Carajás, and **b** Hamersley. Based on data available in Table 1
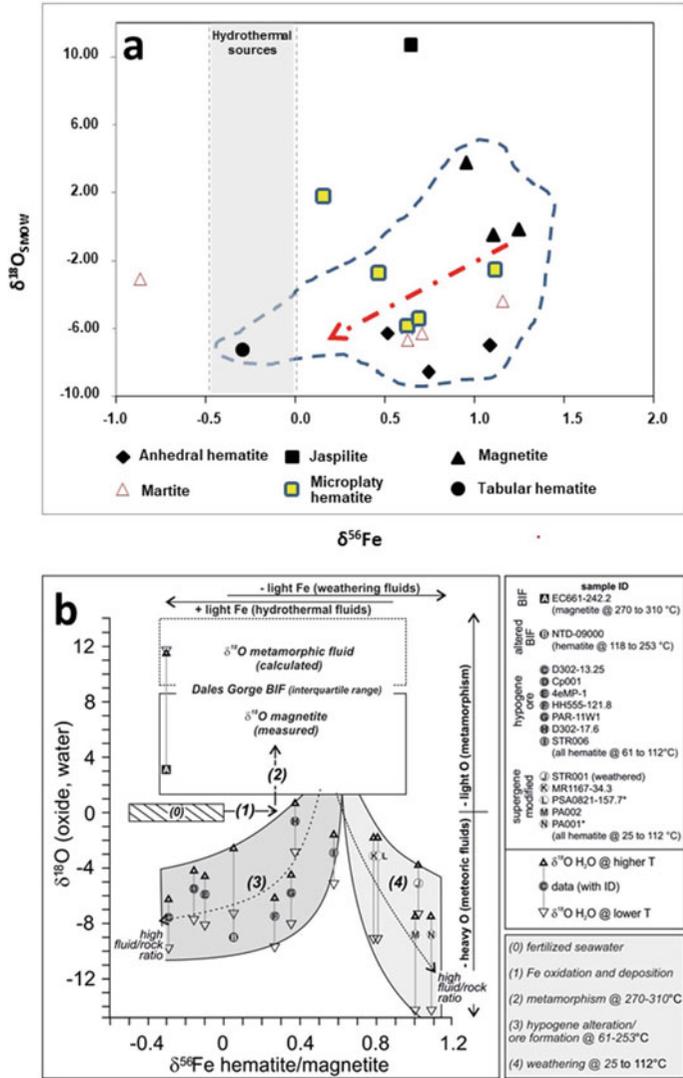
any of the ore samples. Nevertheless, the inclusion of oxygen isotope data allows deducing scenarios of iron isotopic fractionation.

6.3.1 Iron and Oxygen Isotope Pairing

Oxygen isotopes were obtained for a number of samples of the iron isotope data set to investigate the behavior and potential coupling of the Fe–O isotope system during hydrothermal and supergene alteration of BIF and iron ore development.

In order to establish a representative range of Fe–O isotopes for least-altered Dales Gorge BIF, separate published data sets on iron isotopes (Johnson et al. 2008a; Craddock and Dauphas

2011) and oxygen isotopes (Powell et al. 1999) were combined. These data are shown in Table 1 and Fig. 6b, together with published estimates of the pristine Paleoproterozoic seawater isotopic signature.

In unaltered BIF, anchizonal to low-greenschist facies metamorphism (270–310 °C, Becker and Clayton 1976) lead to significant higher δ^{18}O and δ^{56}Fe values, compared to primary seawater signature. In altered BIF and iron ore, the overall δ^{18}O values range from -9 to 0‰ (Table 1, Fig. 6b). This marked difference (δ^{18}O up to 10‰) between the heavy oxygen isotope in metamorphic magnetite in the least-altered BIF

Fig. 7 Distribution of Fe isotope composition of oxides and siderite in iron ores and BIF of different ore deposits from the Hamersley iron district, Australia, including both published and unpublished data (data in Table 1)
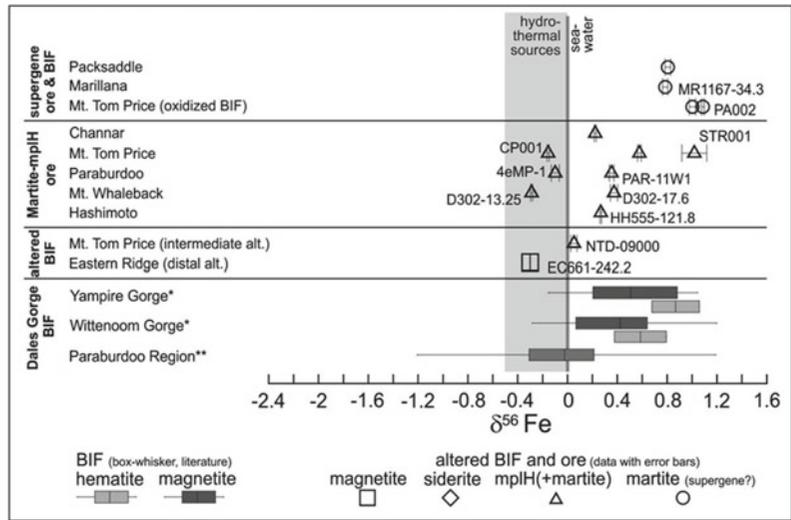
(square in Fig. 6b; Table 1), and hydrothermal hematite (Powell et al. 1999) is in accordance with published data and models of influx of meteoric water depleted in $\delta^{18}O$ during ore formation (Gutzmer et al. 2006; Thorne et al. 2009).

No major shift is shown in iron isotope data, which are indistinguishable from the range of the least-altered BIF. It is, however, interesting to note that a positive correlation exists between $\delta^{18}O$ and $\delta^{56}Fe$ values for most of the hydrothermally altered BIF and ore samples (samples with $\delta^{56}Fe < 0.60$‰; Fig. 6b). For the four supergene modified samples (with $\delta^{56}Fe$ 0.79–1.19‰) the correlation appears to be negative.

Additional Fe–O isotope data also on Hamersley (Dales Gorge member) were combined by Li et al. (2013), who analyzed both magnetite and hematite in BIF. The iron and oxygen isotope signatures highlight a contrasting behavior of these isotopes in the two oxides.

7 Discussion

7.1 Quadrilátero Ferrífero

Although metamorphism did not modify the iron isotope composition of itabirites of the Cauê Formation, hydrothermal fluids related to iron

mineralization generated ores that have somewhat lighter (lower) $\delta^{56}Fe$ ratios with respect to the original protore BIF.

The iron isotope composition of the iron ores is fairly similar to itabirites, suggesting that hydrothermal mineralization did not significantly alter the isotopic composition of the protores. One must also take into account that the chemical attributes of itabirites, the QF protores, no longer reflect those of the original banded iron formation (Harder 1914; Rosière et al. 2008), since modifications were attained via post-depositional alteration and multiple events of metamorphism (Rosière et al. 2008). On the other hand, iron ore iron isotope signatures vary across the QF (Figs. 1a and 3; Mendes et al. 2017), with differences between the western-low and eastern-high strain domains as defined by Rosière et al. (2001).

Mineralization in the western, low-strain domain is mainly characterized by percolation of low-temperature, saline fluids carrying isotopically light Fe(II). Such fluids precipitated ores with new iron oxides, depleted predominantly in ^{56}Fe ($\delta^{56}Fe = -0.80 \pm 0.01$ to -0.13 ± 0.06‰), in open spaces evolved from the leaching of gangue minerals. Ores from this domain have an isotope signature mostly within the interval suggested for 'mineralizing' hydrothermal fluids ($\delta^{56}Fe \approx -0.50$ to 0‰; Rouxel et al.

2005; Markl et al. 2006; Fig. 3). According to Mendes et al. (2017), hydrothermal fluids must have become enriched in light iron isotopes by leaching of Fe(II) from the basement and country rocks (including host BIF), as suggested by Markl et al. (2006), during different stages of the Rhyacian-aged orogeny. The mechanisms of isotope fractionation may have varied in the western-low strain domain. Ores with δ^{56}Fe ratios equivalent to the hydrothermal fluids may have precipitated in equilibrium with these fluids. On the other hand, iron ore with positive δ^{56}Fe ratios is less common. Isotopic heavy iron ore may be a result of kinetic fractionation as a consequence of fast hematite precipitation as indicated by Skulan et al. (2002).

In the eastern, high-strain domain, high-temperature saline fluids, also carrying isotopically light Fe(II), precipitated oxides enriched in heavy iron isotopes. Ores in this domain are enriched in the heavier isotope (δ^{56}Fe = -0.09 ± 0.08 to 0.37 ± 0.06‰; Mendes et al. 2017; Fig. 3), and this may have occurred due to iron isotope fractionation during redox transformation. This resulted in ores less depleted than those of the low-strain domain, and implies that both the isotopic composition of the mineralizing

fluids and the mineralizing conditions differed from those in place in the western domain. Precipitation of hematite under P–T conditions in the higher strain zone may have occurred out of equilibrium with the hydrothermal fluid, resulting in preferential incorporation of the heavy iron isotope into hematite. An alternative suggestion by Mendes et al. (2017) is that positive δ^{56}Fe values of ores could reflect positive kinetic fractionation, resulting from rapid precipitation of hematite. Figure 8 shows that the QF data are compatible with those of the environmentally similar Hamersley BIF and iron ores.

The variation in δ^{56}Fe composition with depth in two drill holes (Fig. 1a) is used by Sampaio et al. (2018) to interpret results in more or less weathered samples, the latter considered to better preserve interaction with a hydrothermal fluid. In one of them (OFS), there is a shift from -0.91‰ at depth to less negative values of -0.60‰ near the surface; the most weathered samples have positive values of 0.30‰ and 1.33‰. In the second hole (GS), δ^{56}Fe increases linearly from -0.11 to 1.23‰ towards the surface, although the most negative values -0.70‰ and -1.16‰ are near the top. The most negative δ^{56}Fe from the OFS can be explained by DIR

Fig. 8 Age versus δ^{56}Fe for all ore data (in Table 1)
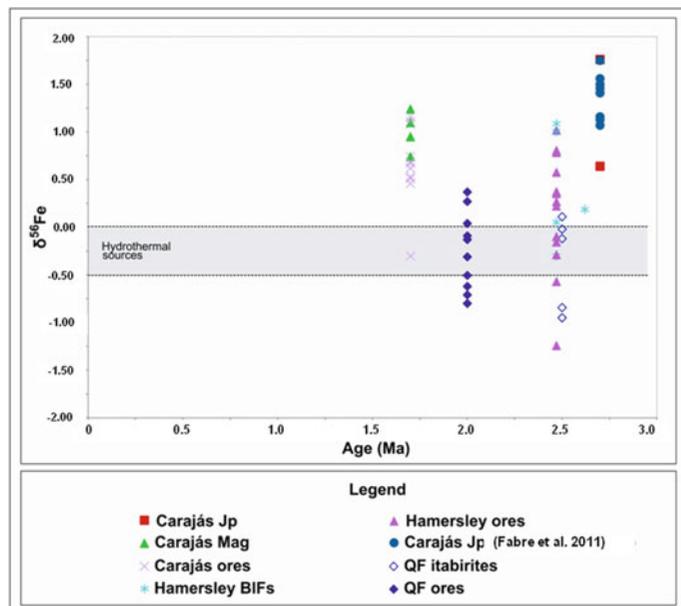
and/or Rayleigh fractionation, while the more positive from the GS may reflect oxidation driven by interaction with a hydrothermal fluid enriched in iron.

7.2 Corumbá

Iron isotope fractionation discussed for the Corumbá BIF are controlled by: (1) the primary seawater isotopic signature, (2) microbial-aided Fe(III) to Fe(II) reduction in the source Fe pool, and (3) supergene Fe(III) to Fe(II) reduction and dissolution. Particular processes responsible for the oxygen isotope fractionation recorded in BIF are: (1) precipitation from seawater; (2) rock dehydration and recrystallization during protracted diagenesis; (3) interaction with hydrothermal alteration fluids during diagenetic gangue dissolution; and (4) interaction with supergene weathering solutions.

Low δ^{56}Fe values between -0.7 and -0.1‰ (Beard et al. 2003; Severmann et al. 2004; Johnson et al. 2008b; Klar et al. 2017) in chert-hematite BIF and hematite mud indicate that a deep ocean seawater was dominated by hydrothermal Fe(II), hence without significant iron isotope fractionation. Precipitation directly from seawater is postulated for the rocks themselves (Klein and Ladeira 2004; Angerer et al. 2016; Viehmann et al. 2016), and thus an oxygen isotope equilibration with seawater signature is likely. The much lower δ^{56}Fe recorded in hematite from carbonate-rich BIF (down to -1.8‰ in sample C-6; Fig. 5) is explained by the temporary increase in low-δ^{56}Fe Fe(II) in the seawater. This low-δ^{56}Fe Fe(II) likely formed by dissimilatory iron reduction (DIR) of an oxidized source prior to BIF precipitation (Beard et al. 1999, 2003), or by abiotic reduction (Balci et al. 2006). Resulting fertilization of the basin with dissolved, isotopically light Fe(II) from a ferric iron-rich substrate would cause an isotopically light Fe-hydroxide precipitate in BIF. The Fe source in which DIR takes place could be weathered sedimentary rocks or BIF in the stratigraphic footwall. According to this model, microbial activity and associated fractionation by

about -0.3 to -1.3‰ was highest shortly before and during precipitation of carbonate-rich BIF (Angerer et al. 2016). Carbonate spheroids in carbonate BIF layers are discussed as biogenic relics, and thus support microbiological activity in the basin (Angerer et al. 2016).

Late diagenesis occurred between ~ 100 and 180 °C, according to the hematite-quartz pair thermometer (Hoefs et al. 1987). Non-equilibrium oxygen isotope fractionation is reflected in a range of oxygen isotope data (samples C-6, C-11, C-14; Fig. 5). In contrast to oxygen isotopes, diagenesis does not seem to have any significant effect on the primary (i.e., hydrothermal and DIR influenced seawater) Fe-isotope fractionation, although a general possibility has been discussed by several authors (Johnson et al. 2008b; Kunzmann et al. 2017, and references therein). The observed negative Fe–O isotope correlation (Fig. 5) must be interpreted as a coincidental result of two distinct (decoupled) fractionation processes.

During a late diagenetic hydrothermal overprint, silica and carbonate dissolution caused small-scale upgrade to high-grade laminated hematite ore (Angerer et al. 2016). Hydrothermal alteration took place under fluid temperatures of 100–250 °C (Angerer et al. 2016). Based on the estimated temperature range, calculated $\delta^{18}O_{water}$ of fluids ranges between -2 and $+4$‰, respectively. Iron isotopes remain unfractionated (δ^{56}Fe $\pm$ 0‰) during this syn-diagenetic hydrothermal alteration (see laminated hematite ore in Fig. 3). Diagenetic re-equilibration of oxygen isotopes of hematite were accommodated by recrystallization, hence Fe_2O_3 redistribution at the microscale (Angerer et al. 2016). The contrasting lack of iron isotope fractionation shows that Fe_2O_3 behaved as an immobile component at the rock scale during these processes. The decoupled nature of isotopic fractionation is, therefore, a result of the different scales of mobility of oxygen and iron.

Iron isotope fractionation occurred during supergene alteration. Hematite from goethite-altered BIF shows heavier ^{56}Fe (0.76‰), compared to unweathered BIF and laminated ore. This indicates that hematite was not chemically

inert during weathering. Abundant micro-porosity in the hematite matrix of saprolitic BIF indicates not only dissolution of silica and carbonate, but also partial dissolution of hematite. It is inferred that ^{56}Fe hematite represents a residue after preferential dissolution of ^{54}Fe. This is in accordance with the established understanding that weathering solutions have commonly light iron isotopes as a result of Fe(II) dissolution (Fantle and DePaolo 2004; Bergquist and Boyle 2006; Ingri et al. 2006). Weathering causes significant fractionation also of oxygen isotopes, where $\delta^{18}O$ values decrease by equilibration with the meteoric fluid (Fig. 5). The coupling of ^{56}Fe and ^{18}O isotopes supports the involvement of characteristically light oxygen-enriched and heavy iron-depleted supergene fluids.

7.3 Carajás

There is a general tendency for $\delta^{56}Fe$ of the Archean jaspilites from Carajás to show higher values (Figs. 4 and 6a) compared to hematite ores, particularly those of late paragenetic stage (Fig. 2e; Figueiredo e Silva et al. 2013). The iron isotope data for protore BIF (jaspilites) coincide with the heaviest $\delta^{56}Fe$ ore values (Fig. 4), suggesting that fluid evolution and mineralization did not alter significantly the iron isotope composition of the original oxides. However, a slight trend towards negative values exists from the early-stage magnetite to the latest tabular (Fig. 2e) hematite, indicating some fractionation during advanced ore mineralization, probably due to high influx of hydrothermal fluid in the waning mineralization stages.

Considering the dual magmatic-meteoric hydrothermal fluid flow model for Carajás (Figueiredo e Silva et. al. 2013; Hagemann et al. 2016), it is worth mentioning the study by Wawryk and Foden (2015). Wawryk and Foden (2015) show that oxidized magmas crystallize magmatic magnetite, which sequesters heavy Fe thus producing an isotopically light magmatic-hydrothermal fluid. This may explain the lower $\delta^{56}Fe$ of the Carajás ore samples, compared to protore BIF, as observed in Figs. 4 and 8.

The advanced alteration stage in high-grade ore displays the most depleted $\delta^{18}O$ and $\delta^{56}Fe$ values (Fig. 6a) and may represent the highest fluid-rock ratio during hydrothermal alteration as suggested by Figueiredo e Silva et al. (2013). This depletion is interpreted to result from the progressive mixture of descending, heated meteoric water with ascending modified magmatic fluids.

7.4 Hamersley

At first sight, martite-microplaty hematite ore $\delta^{56}Fe$ isotopes (2nd row Fig. 7; − 0.29 to + 1.02‰) are indistinguishable from the range of the least-altered BIF (3rd and 4th rows; Fig. 7) suggesting no significant fractionation throughout microplaty hematite ore formation. However, pairing of iron with oxygen isotope data reveals cryptic iron isotope fractionation trends.

The interquartile range of magnetite $\delta^{56}Fe$, in the least-altered Dales Gorge Member BIF (from different localities) (Fig. 7), is from − 0.3 to + 0.9‰ (Fig. 7). The data set of Steinhoefel et al. (2010) from adjacent microbands in one sample (− 0.94 to − 0.82‰, average − 0.87‰) indicates that isotopic variability is low at the sample scale. However, in comparison with the other available data (Johnson et al. 2008a; Craddock and Dauphas 2011), it is evident that the variability of $\delta^{56}Fe$ values is high at the stratigraphic or regional scale. As yet, the reasons for this spread of iron isotopes in BIF are not fully understood (see "Brief summary on iron isotopes" section for references to literature focusing on isotope data related to BIF deposition).

While the prominent variability of iron isotope values in BIF, with a general shift towards heavier signature compared to seawater, most likely resulted from Fe source-related and depositional processes, it is unlikely that low-grade metamorphism changed significantly the iron isotopic budget of BIF. This is because Fe(III) reduction associated with hematite to magnetite replacement forming metamorphic assemblages cannot produce heavier isotope values (Fe reduction always decreases $\delta^{56}Fe$; e.g., Beard

et al. 1999, 2003). In contrast to iron isotopes, the oxygen isotopic signatures in magnetite are strongly dependent on metamorphic equilibration. In consequence, during deposition of BIF (see stage 1 arrow in Fig. 6b) and metamorphism (stage 2 arrow) iron and oxygen isotopes are not coupled.

However, this contrasts with subsequent carbonate-hematite alteration and hematite ore formation in BIF (Fig. 6b). Although any systematic modification of iron isotopes in ore is obscured by the large variety of $\delta^{56}Fe$ in least-altered BIF, a positive correlation between $\delta^{18}O$ and $\delta^{56}Fe$ (trend 3 arrow Fig. 6b) is evidence of significant fractionation towards lower isotopic values. Light $\delta^{18}O$ signatures of iron oxides result from intense meteoric water influx (Gutzmer et al. 2006), and isotopic equilibration with the ambient water, i.e., lowest values, is most complete in zones of highest fluid-rock interaction, for instances near ore-controlling structures (Thorne et al. 2009). The observed covariance of $\delta^{56}Fe$ with decreasing $\delta^{18}O$ thus means that iron isotope equilibration takes place during ore formation and is (as $\delta^{18}O$) dependent on the intensity of fluid-rock interaction. According to Saunier et al. (2011), there is no iron isotope fractionation between hydrothermal fluid and precipitated hematite below 200 °C. The iron for microplaty hematite, locally sourced from dissolved iron oxides, Fe-rich carbonates and silicates, is thus characterized by ferrous Fe with low $\delta^{56}Fe$ values. Based on a carbonate-altered BIF (sample no. B, Fig. 6b), it can be speculated that hot basinal brines, which caused such carbonate alteration (Barley et al. 1999; Hagemann et al. 1999; Taylor et al. 2001; Thorne et al. 2004), were low in $\delta^{56}Fe$ and $\delta^{18}O$, and thus developed light isotopic signatures in carbonates and oxides prior to the meteoric fluid flow. Alternatively, or additionally, incongruent dissolution/removal of heavy iron from Fe-rich phases during oxidation and hematite mineralization also caused low $\delta^{56}Fe$ values in iron ore samples. The latter fractionation process is invoked for magnetite oxidation, i.e., martisation in ore. Although the involved meteoric water, at temperature of ∼ 80–100 °C and low

salinities (Thorne et al. 2008), cannot be very rich in iron, the fluid seems to be able to fractionate iron isotopes. In order to achieve this, mineral-fluid exchange of iron during protracted metasomatism at very high-fluid rock ratios is crucial. A similarly directed Fe–O trend in the Carajás hydrothermal hematite set (Fig. 6a) is striking and implies a Fe–O isotope coupling. However, this trend is formed by temporarily distinct (early to late) hematite stages and is thus discussed separately (see above). The Corumbá BIF samples, on the other hand, are characterized by disequilibrium during early microbial and late diagenetic hydrothermal processes and thus largely recorded uncoupled iron and oxygen isotope signatures.

Comparing the two Paleoproterozoic examples, QF and Hamersley, the range of $\delta^{56}Fe$ values are similar, and most host BIFs and hypogene iron ores fall within related ranges (Figs. 3, 7 and 8). In the Hamersley Province a two-stage model is invoked (Barley et al. 1999; Hagemann et al. 1999; Taylor et al. 2001; Thorne et al. 2004), and in the QF region Hensler et al. (2015) proposed a dual basinal-meteoric fluid mixing model. Mixing of meteoric fluids with deeper crustal brines is also implied for hematite precipitation in the Triassic Schwarzwald hydrothermal vein deposits (Germany), where $\delta^{56}Fe$ values range from − 0.49 to + 0.53 (Markl et al. 2006). This range partly overlaps those of the QF (− 0.80 to 0.37‰, excluding specularite) and Hamersley (− 0.30 to + 1.10‰) iron ores.

In contrast to the hydrothermal hematite stage, supergene-modified ore samples reveal a negative correlation of $\delta^{18}O$ and $\delta^{56}Fe$ (trend 4 arrow Fig. 6b). Hematite experienced isotopic fractionation to heavy Fe during incongruent dissolution of preferable light ^{56}Fe. The resulting weathering solutions are enriched in light iron isotopes (Fantle and DePaolo 2004; Bergquist and Boyle 2006; Ingri et al. 2006). This supergene fractionation process is the same one that has been inferred for goethite-altered Corumbá ore.

In summary, while oxygen fractionation follows a trend of decrease for both hydrothermal and supergene alteration, iron isotope fractionation shows marked differences: $\delta^{56}Fe$ decreases

during hydrothermal alteration and increases during supergene alteration. The observed correlations suggest that during hypogene and supergene alteration processes, oxygen and iron isotope fractionations are coupled, and that fluid/rock ratios play significant roles for the magnitude of fractionation.

8 Conclusions

Based on iron isotope data, and coupled iron and oxygen isotope signatures of BIF-hosted iron ores from the iron districts considered in this contribution (Table 1), distributed in space and time, the following conclusions can be inferred:

1. Archean, jaspilite-hosted Carajás hypogene ores tend to display lower δ^{56}Fe values than their host BIF counterparts (Fig. 4). There is a correlation between coupled iron and oxygen isotope through the paragenetic sequence, progressively towards lower isotopic values, especially for δ^{18}O (Fig. 6a).

2. The Carajás (+ 1.16 to − 0.30‰) and the Paleoproterozoic Hamersley (+ 1.02 to − 0.29‰) hypogene ores display similar δ^{56}Fe intervals (Figs. 4 and 7). Ores from the Quadrilátero Ferrífero (QF) Paleoproterozoic Cauê Formation show a tendency towards lower values from + 0.37 to − 0.80‰ (Fig. 3).

3. In the Hamersley deposits, iron ore and hydrothermally modified BIF show a positive correlation between δ^{18}O and δ^{56}Fe (Fig. 6b), indicating that iron and oxygen isotope fractionation took place during oxidized meteoric water influx with variable fluid/rock ratios. In contrast, supergene-modified samples are characterized by a negative correlation of δ^{18}O and δ^{56}Fe, implying isotope coupling under distinct fluid-rock processes.

4. Quartz and carbonate itabirites from the QF have iron isotope signatures as a result of their distinct positioning in the depositional basin. The latter, with lower δ^{56}Fe ratios, is inferred to be more distal from the iron source than the former (Fig. 3).

5. The range in δ^{56}Fe values of hypogene iron ores is similar to that of the QF itabirites (Fig. 3). The iron isotope variations for the QF iron ores are better depicted when data are compared between the western, low-strain and the eastern, high-strain deformation domains, probably reflecting the different physical–chemical characteristics of the involved saline fluids that carried isotopically light Fe(II). Percolation of low-temperature fluids dominated the western domain, whereas the eastern domain was typified by high-temperature fluids. Precipitated oxides of this latter domain became enriched in the heavy iron isotopes due to iron isotope fractionation during redox transformation, resulting in ores less depleted than those of the low-strain domain.

6. Two processes controlled the iron isotopes in the Corumbá BIF (Fig. 3): a deep ocean seawater signature, characterized by a hydrothermal Fe fertilization, and a microbial or abiotic reduction in the iron source. This resulted in the formation of BIF with both non-fractionated δ^{56}Fe (± 0‰) and low δ^{56}Fe (− 0.5 to − 1.7‰; also Fig. 5). Local, diagenetic hydrothermal silica dissolution is reflected in the oxygen isotope data, but not in the iron isotope fractionation. Iron and oxygen isotope are coupled in the supergene stage: δ^{56}Fe values increase, while δ^{18}O values decrease (Fig. 5). This supports the involvement of light oxygen isotope-enriched and heavy iron isotope-depleted weathering solutions.

7. Overall, and despite all local differences, there is a general tendency for BIF δ^{56}Fe data to display moderately heavier values for all deposits compared to hypogene ores, which tend to shift towards slightly lower values. Direct coupling with oxygen isotopic values observed in Carajás, Hamersley, and Corumbá, indicate that δ^{56}Fe is a sensitive recorder for the intensity and type of fluid-rock interaction: lowest values are recorded in rocks of highest fluid-rock ratios during hydrothermal alteration and highest values are recorded in rocks of highest fluid-rock ratios during supergene/weathering alteration.

9   Implications for Exploration

The application of iron isotope in exploration is presently limited, although some promising applications are here indicated. For example, the correlation of increasing light oxygen and iron isotopes towards zones of high fluid-rock ratios may assist in targeting concealed shear zones, which could have acted as a significant fluid plumbing system, thereby facilitating the upgrade of BIF to high grade iron ore. Hand samples or drill core material from early, reconnaissance mapping or drilling could be analyzed for oxygen and iron isotopes. Any depleted values, when compared to least-altered BIF or itabirites, could be plotted into a geological map and contours of equal isotope values or ranges that may identify zones of oxygen and iron isotope depletion, hence increased hydrothermal fluid flow.

10   Future Work

Iron isotope studies in ore deposits have only been applied recently. Therefore, only limited case studies of iron isotopes in ore deposits or mineral systems have been conducted (e.g., Markl et al. 2006; Wang et al. 2011; Bilenker 2015; Santiago 2016). Most iron isotope studies have been applied to BIF systems where the redox environment is constrained and the potential for bacterial Fe(III) reduction has been established (Beard and Johnson 2004). Recently, Mendes et al. (2017) showed that the iron isotope composition of iron ore minerals varies systematically between deformational domains in the QF of Brazil. These authors link fluid temperatures and composition to different δ^{56}Fe values. By analogy, the δ^{56}Fe isotopic composition of iron oxide minerals in other iron ore systems hosted in itabirite, such as at Simandou (Guinea; Cope et al. 2008), could be analyzed in order to test whether metamorphism, or the lack thereof, and deformation in these deposits is linked to specific hydrothermal fluids, and whether δ^{56}Fe may be used to monitor and constrain such fluids. Iron isotope studies could be easily expanded to iron-oxide-copper–gold (IOCG) and iron-oxide-

apatite (IOA) systems, where magnetite is a common alteration and, in rare cases, also an ore mineral. Some data are available in Santiago (2016) for IOCG deposits, and in Weis (2013), Weis et al. (2013), Bilenker (2015), Bilenker et al. (2016), Childress et al. (2016) Knipping et al. (2019), Troll et al. (2019) for IOA deposits.

Although many studies of IOCG systems have linked the origin of Cu to magmatic hydrothermal fluids (Williams et al. 2005a), the origin of Fe is largely unknown. Orogenic gold systems, in certain host rocks, contain magnetite as a characteristic hydrothermal alteration mineral, specifically in distal alteration zones (e.g., at the giant Golden Mile in Western Australia). Here the redox environment could be (better) constrained during hydrothermal fluid flow in distal portion of the ore system. Furthermore, in distal alteration zones of orogenic gold systems, the δ^{56}Fe composition of magnetite could be differentiated from that of the disseminated orthomagmatic magnetite, in host rock basalt or metamorphic equivalent, or metamorphosed syngenetic magnetite in gold-associated BIF deposits. Hydrothermal magnetite through fluid-rock interaction would produce fluids that have lower δ^{56}Fe values when compared to the orthomagmatic magnetite. In ancient, now land-based, volcanic-hosted massive sulfide systems, iron isotopes could be applied to vent fluids in order to better constrain the origin of the fluids, particularly the origin of iron in the various sulfides that characterize these systems.

References

Alkmim FF, Marshak S (1998) Transamazonian orogeny in the southern São Francisco craton region, Minas Gerais, Brazil: evidence for Paleoproterozoic collision and collapse in the Quadrilátero Ferrífero. Precambrian Res 90:29–58

Anbar AD, Rouxel O (2007) Metal stable isotopes in paleoceanography. Annu Rev Earth Planet Sci 35:717–746

Anbar AD, Jarzecki AA, Spiro TG (2005) Theoretical investigation of iron isotope fractionation between Fe $(H_2O)_6^{3+}$ and $Fe(H_2O)_6^{2+}$: implications for iron stable isotope geochemistry. Geochim Cosmochim Acta 69:825–837

Angerer T, Hagemann SG, Danyushevsky LV (2012) Geochemical evolution of the banded iron formation-hosted high-grade iron ore system in the Koolyanobbing greenstone belt, Western Australia. Econ Geol 107:599–644

Angerer T, Duuring P, Hagemann SG, Thorne W, McCuaig TC (2014) A mineral system approach to iron ore in Archaean and Palaeoproterozoic BIF of Western Australia. Geol Soc London Spec Publ 393:81–115

Angerer T, Hagemann SG, Walde DN, Halverson GP, Boyce AJ (2016) Multiple metal sources in the glaciomarine facies of the Neoproterozoic Jacadigo iron formation in the "Santa Cruz deposit", Corumbá, Brazil. Precambrian Res 275:369–393

Balci N, Bullen TD, Witte-Lien K, Shanks WC, Motelica M, Mandernack KW (2006) Iron isotope fractionation during Fe(II) oxidation and Fe(III) precipitation microbially stimulated. Geochim Cosmochim Acta 70:622–639

Baltazar OF, Lobato LM (2020) Structural evolution of the Rio das Velhas greenstone belt, Quadrilátero Ferrífero Brazil: influence of Proterozoic orogenies on its western Archean gold deposits. Minerals 10:1–38

Barley ME, Pickard AL, Hagemann SG, Folkert SL (1999) Hydrothermal origin for the 2 billion year old Mount Tom Price giant iron ore deposit, Hamersley Province, Western Autralia. Miner Deposita 34:784–789

Beard BL, Johnson CM (2004) Inter-mineral Fe isotope variations in mantle-derived rocks and implications for the Fe geochemical cycle. Geochim Cosmochim Acta 68:4727–4743

Beard BL, Johnson CM, Cox L, Sun H, Nealson KH, Aguilar C (1999) Iron isotope biosignatures. Science 285:1889–1892

Beard BL, Johnson CM, Von Damm KL (2003) Iron isotope constraints on Fe cycling and mass balance in oxygenated Earth oceans. Geology 31:629–632

Becker RN, Clayton RN (1976) Oxygen isotope study of a Precambrian banded iron-formation, Hamersley Range, Western Australia. Geochim Cosmochim Acta 40:1153–1165

Bergquist BA, Boyle EA (2006) Iron isotopes in the Amazon River system: weathering and transport signatures. Earth Planet Sci Lett 248:54–68

Bilenker LD (2015) Elucidating igneous and ore-forming processes with iron isotopes by using experimental and field-based methods. Unpublished PhD thesis, The University of Michigan

Bilenker LD, Simon AC, Reich M, Lundstrom CC, Gajos N, Bindeman IN, Barra F, Munizaga F (2016) Fe-O stable isotope pairs elucidate a high-temperature origin of Chilean iron oxide-apatite deposits. Geochim Cosmochim Acta 177:94–104

Busigny V, Planavsky NJ, Jézéquel D, Crowe S, Louvat P, Moureau J, Viollier E, Lyons TW (2014) Iron isotopes in an Archean ocean analogue. Geochim Cosmochim Acta 133:443–462

Busigny V, Planavsky NJ, Goldbaum E, Lechte MA, Feng L, Lyons TW (2018) Origin of the Neoproterozoic Fulu iron formation, South China: insights from iron isotopes and rare earth element patterns. Geochim Cosmochim Acta 242:123–142

Childress TM, Simon AC, Day WC, Lundstrom CC, Bindeman IN (2016) Iron and oxygen isotope signatures of the Pea Ridge and Pilot Knob magnetite-apatite deposits, Southeast Missouri, USA. Econ Geol 111:2033–2044

Clout JMF (2005) Iron formation-hosted iron ores in the Hamersley Province of Western Australia. In: Iron Ore Conference 2005, Fremantle, WA, pp 19–21

Cope IL, Wilkinson JJ, Boyce AJ, Chapman JB, Herrington RJ, Harris CJ (2008) Genesis of the Pic de Fon iron oxide deposit, Simandou Range, Republic of Guinea, West Africa. Rev Econ Geol 15:339–360

Cox GM, Halverson GP, Minarik WG, Le Heron DP, Macdonald FA, Bellefroid EJ, Strauss JV (2013) Neoproterozoic iron formation: An evaluation of its temporal, environmental and tectonic significance. Chem Geol 362:232–249

Cox GM, Halverson GP, Poirier A, Le Heron D, Strauss JV, Stevenson R (2016) A model for Cryogenian iron formation. Earth Planet Sci Lett 43:280–292

Craddock PR, Dauphas N (2011) Iron and carbon isotope evidence for microbial iron respiration throughout the Archean. Earth Planet Sci Let 303:121–132

Crosby H, Johnson C, Roden E, Beard B (2005) Coupled Fe(II)–Fe(III) electron and atom exchange as a mechanism for Fe isotope fractionation during dissimilatory iron oxide reduction. Envir Sci Tech 39:6698–6704

Crosby HA, Roden EE, Johnson CM, Beard BL (2007) The mechanisms of iron isotope fractionation produced during dissimilatory Fe(III) reduction by *Shewanella putrefaciens* and *Geobacter sulfurreducens*. Geobiology 5:169–189

Czaja AD, Johnson CM, Beard BL, Roden EE, Li W, Moorbath S (2013) Biological Fe oxidation controlled deposition of banded iron formation in the ca. 3770 Ma Isua Supracrustal Belt (West Greenland). Earth Planet Sci Lett 363:192–203

Dai Y, Zhu Y, Lianchang Z, Mingtian Z (2017) Meso- and Neoarchean banded iron formations and genesis of high-grade magnetite ores in the Anshan-Benxi Area, North China Craton. Econ Geol 112:1629–1651

Dalstra HJ, Rosière CA (2008) Structural controls on high-grade iron ores hosted by banded iron formation: a global perspective. Rev Econ Geol 15:73–106

Dauphas N, Rouxel O (2006) Mass spectrometry and natural variations of iron isotopes. Mass Spectr Rev 25:515–550

Dauphas N, van Zuilen M, Wahwa M, Davis AM, Marty B, Janney PE (2004) Clues from Fe isotope variations on the origin of early Archean BIFs from Greenland. Science 306:2077–2080

Dauphas N, Seth GJ, Rouxel O (2017) Iron isotope systematics. Rev Mineral Geochem 82:415–510

DOCEGEO (Rio Doce Geologia e Mineração S.A.) (1988) Revisão litoestratigráfica da Província Mineral de Carajás. In: Anais do XXXVI Congresso Brasileiro de Geologia, Belém, Brazil, Anexo, p 11–54

Dorr JVN (1945) Manganese and iron deposits of Morro do Urucum, Mato Grosso, Brazil. US Geol Surv Bull 946A:1–47

Dorr JVN (1969) Physiographic, stratigraphic and structural development of the Quadrilátero Ferrífero, Minas Gerais. US Geol Surv Prof Pap 641-A:110

Fabre S, Nédélec A, Poitrasson F, Strauss H, Thomazo C, Nogueira A (2011) Iron and sulphur isotopes from the Carajás mining province (Pará, Brazil): implications for the oxidation of the ocean and the atmosphere across the Archaean-Proterozoic transition. Chem Geol 289:124–139

Fantle MS, DePaolo DJ (2004) Iron isotopic fractionation during continental weathering. Earth Planet Sci Lett 228:547–562

Figueiredo e Silva RC, Lobato LM, Rosière CA (2008). A hydrothermal origin for the jaspilite-hosted giant Sierra Norte deposits in the Carajás Mineral Province, Pará State, Brazil. Rev Econ Geol 15:255–290

Figueiredo e Silva RC, Hagemann SG, Lobato LM, Rosière CA, Banks DA, Davidson GJ, Vennemann T, Hergt J (2013) Hydrothermal fluid processes and evolution of the giant Serra Norte jaspilite-hosted iron ore deposits, Carajás Mineral Province, Brazil. Econ Geol 108:739–779

Freitas BT, Warren LV, Boggiani PC, de Almeida RP, Piacentini T (2011) Tectono-sedimentary evolution of the Neoproterozoic BIF-bearing Jacadigo Group, SW-Brazil. Sedim Geol 238:48–70

Frost CD, von Blanckenburg F, Schoenberg R, Frost BR, Swapp SM (2007) Preservation of Fe isotope heterogeneities during diagenesis and metamorphism of banded iron formation. Contrib Mineral Petrol 153:211–235

Gaucher C, Sial AN, Frei R (2015) Chemostratigraphy of Neoproterozoic banded iron formation (BIF): types, age and origin. In: Ramkumar M (ed) Chemostratigraphy, concepts, techniques and applications. Elsevier, Amsterdam, pp 433–499

Gutzmer J, Mukhopadhyay J, Beukes NJ, Pack A, Hayashi K, Sharp ZD (2006) Oxygen isotope composition of hematite and genesis of high-grade BIF-hosted iron ores. Geol Soc Am Mem 198:257–268

Hagemann SG, Barley ME, Folkert SL, Yardley BBW, Banks DA (1999) A hydrothermal origin for the giant BIF-hosted Tom Price iron ore deposit. In: Stanley CJ (ed) Mineral Deposits—Process to Processing. Balkema, Rotterdam, pp 41–44

Hagemann SH, Angerer T, Duuring P, Rosière CA, Figueiredo e Silva RC, Lobato LM, Hensler AS, Walde DHG. BIF-hosted iron mineral system: a review (2016). Ore Geol Rev 76:317–359

Halverson GP, Poitrasson F, Hoffman PF, Nédélec A, Montel JM, Kirby J (2011) Fe isotope and trace element geochemistry of the Neoproterozoic synglacial Rapitan iron formation. Earth Planet Sci Lett 309:100–112

Harder EC (1914) The "Itabirite" iron ores of Brazil. Econ Geol 9:101–111

Hasui Y, Almeida F (1970) Geocronologia do centro-oeste brasileiro. Boletim Da Sociedade Brasileira De Geologia 19:5–26

Hensler AS, Hagemann SG, Rosière CA, Angerer T, Gilbert S (2015) Hydrothermal and metamorphic fluid-rock interaction associated with hypogene hard iron ore mineralization in the Quadrilátero Ferrífero, Brazil: Implications from in-situ laser ablation ICP-MS iron oxide chemistry. Ore Geol Rev 69:325–351

Hoefs J, Müller G, Schuster KA, Walde D (1987) The Fe-Mn ore deposits of Urucum, Brazil: an oxygen isotope study. Chem Geol Isotope Geoscience Section 65:311–319

Hoffman PF, Macdonald FA, Halverson GP (2011) Chemical sediments associated with Neoproterozoic glaciation: iron formation, cap carbonate, barite and phosphorite. Geol Soc London Mem 36:67–80

Holland HD (2006) The oxygenation of the atmosphere and oceans. Philos Trans R Soc Lond B Biol Sci 361 (1470):903–915

Horn I, von Blanckenburg F, Schoenberg R, Steinhoefel G, Markl G (2006) In situ iron isotope ratio determination using UV-femtosecond laser ablation with application to hydrothermal ore formation processes. Geochim Cosmochim Acta 70:3677–3688

Ingri J, Malinovsky D, Rodushkin I, Baxter DC, Widerlund A, Andersson P, Gustafsson O, Forsling W, Öhlander B (2006) Iron isotope fractionation in river colloidal matter. Earth Planet Sci Lett 245:792–798

Jacobsen SB, Kaufman AJ (1999) The Sr, C and O isotopic evolution of Neoproterozoic seawater. Chem Geol 161:37–57

Johnson CM, Beard B (2006) Fe isotopes: an emerging technique in understanding modern and ancient biogeochemical cycles. GSA Today 16:4–10

Johnson CM, Skulan JL, Beard BL, Sun H, Nealson KH, Braterman PS (2002) Isotopic fractionation between Fe(III) and Fe(II) in aqueous solutions. Earth Planet Sci Lett 195:141–153

Johnson CM, Beard BL, Beukes NJ, Klein C, O'Leary JM (2003) Ancient geochemical cycling in the Earth as inferred from Fe isotope studies of banded iron formations from the Transvaal Craton. Contrib Mineral Petrol 144:523–547

Johnson CM, Beard BL, Albarède F (eds) (2004) Geochemistry of non-traditional stable isotopes. Rev Mineral 55, 454 p

Johnson CM, Roden EE, Welch SA, Beard BL (2005) Experimental constraints on Fe isotope fractionation during magnetite and Fe carbonate formation coupled to dissimilatory hydrous ferric oxide reduction. Geochim Cosmochim Acta 69:963–993

Johnson CM, Beard BL, Klein C, Beukes NJ, Roden EE (2008a) Iron isotopes constrain biologic and abiologic processes in banded iron formation genesis. Geochim Cosmochim Acta 72:151–169

Johnson CM, Beard BL, Roden EE (2008b) The iron isotope fingerprints of redox and biogeochemical cycling in modern and ancient. Annu Rev Earth Planet Sci 36:457–493

Klar JK, Homoky WB, Statham PJ, Birchill AJ, Harris EL, Woodward EMS, Silburn B, Cooper MJ, James RH, Connelly DP, Chever F, Lichtschlag A, Graves C (2017) Stability of dissolved and soluble Fe(II) in shelf sediment pore waters and release to an oxic water column. Biogeochemistry 135:49–67

Klein C (2005) Some Precambrian banded iron-formations (BIFs) from around the world: their age, geologic setting, mineralogy, metamorphism, geochemistry, and origin. Am Mineral 90:1473–1499

Klein C, Ladeira EA (2004) Geochemistry and mineralogy of Neoproterozoic banded iron formations and some selected, siliceous manganese formations from the Urucum District, Mato Grosso do Sul, Brazil. Econ Geol 99:1233–1244

Knipping JL, Fiege A, Simon AC, Oeser M, Reich M, Bilenker LD (2019) In-situ iron isotope analyses reveal igneous and magmatic-hydrothermal growth of magnetite at the Los Colorados Kiruna-type iron oxide-apatite deposit, Chile. Am Min 104:471–484

Krapež B, Barley ME, Pickard AL (2003) Hydrothermal and resedimented origins of the precursor sediments to banded iron formation: sedimentological evidence from the Early Palaeoproterozoic Brockman Supersequence of Western Australia. Sedimentology 50:979–1011

Kunzmann M, Gibson TM, Halverson GP, Malcolm SWH, Bui TH, Carozza DA, Sperling EA, Poirier A, Cox GM, Wing BA (2017) Iron isotope biogeochemistry of Neoproterozoic marine shales. Geochim Cosmochim Acta 209:85–105

Lantinka ML, Oonka PBH, Floor GH, Tsikos H, Mason PRD (2018) Fe isotopes of a 2.4 Ga hematite-rich IF constrain marine redox conditions around the GOE. Precambrian Res 305:218–235

Lascelles DF (2006) The genesis of the Hope Downs iron ore deposit, Hamersley Province, western Australia. Econ Geol 101:1359–1376

Levasseur S, Frank M, Hein JR, Halliday AN (2004) The global variation in the iron isotope composition of marine hydrogenetic ferromanganese deposits: implications for seawater chemistry? Earth Planet Sci Lett 224:91–105

Li W, Huberty JM, Beard BL, Kita NT, Valley JW, Johnson CM (2013) Contrasting behavior of oxygen and iron isotopes in banded iron formations revealed by *in situ* isotopic analysis. Earth Planet Sci Lett 384:132–143

Li X, Wang J, Wang H (2017) Fe Isotopic compositions of modern seafloor hydrothermal systems and their influence factors. J Chem 2017:1417302. https://doi.org/10.1155/2017/1417302

Lobato LM, Figueiredo e Silva RC, Hagemann SG, Thorne WS, Zucchetti M, (2008) Hypogene alteration associated with high-grade banded iron formation-related iron ore. Rev Econ Geol 15:107–128

Lovley DR, Holmes DE, Nevin K (2004) Dissimilatory Fe(III) and Mn(IV) reduction. Adv Microb Physiol 49:219–286

Markl G, von Blanckenburg F, Wagner T (2006) Iron isotope fractionation during hydrothermal ore deposition and alteration. Geochim Cosmochim Acta 70:3011–3030

Mendes MCO, Lobato LM, Halverson GP, Kunsmann M, Rosière CA (2017) Iron isotope and REE+Y composition of the Paleoproterozoic banded iron formations and their related iron ores from the Quadrilátero Ferrífero, Brazil: Implications for their genesis. Mineral Deposita 52:159–180

Morris RC (1983) Supergene alteration of banded iron-formation. In: Trendall AF, Morris RC (eds) Iron-formation: facts and problems. Elsevier, Amsterdam, pp 513–534

Morris RC (1985) Genesis of iron ore in banded iron-formation by supergene and supergene-metamorphic processes; a conceptual model. In: Handbook of strata-bound and stratiform ore deposits vol 13, pp 73–235

Morris RC (2002) Genesis of high grade hematite orebodies of the Hamersley Province, Western Australia—a discussion. Econ Geol 97:177–181

Morris RC, Horwitz RC (1983) The origin of the iron-formation-rich Hamersley Group of Western-Australia —Deposition on a platform. Precambrian Res 21:273–297

Morris RC, Fletcher AB (1987) Increased solubility of quartz following ferrous-ferric iron reactions. Nature 330:250–252

Morris RC, Thornber MR, Ewers WE (1980) Deep-seated iron ores from banded iron-formation. Nature 288:250–252

Piacentini T, Vasconcelos PM, Farley KA (2013) $^{40}Ar/^{39}Ar$ constraints on the age and thermal history of the Urucum Neoproterozoic banded iron-formation, Brazil. Precambrian Res 228:48–62

Pires FRM (1995) Textural and mineralogical variations during the metamorphism of the Proterozoic Itabira

iron formation in the Quadrilátero Ferrífero, Minas Gerais, Brazil. An Acad Bras Ciênc 67:77–105

Planavsky NJ, Rouxel OJ, Bekker A, Hofmann A, Little CTS, Lyons TW (2012) Iron isotope composition of some Archean and Proterozoic iron formations. Geochim Cosmochim Acta 80:158–169

Poitrasson F (2006) On the iron isotope homogeneity level of the continental crust. Chem Geol 235:195–200

Powell CM, Oliver NHS, Li ZX, Martin DM, Ronaszeki J (1999) Synorogenic hydrothermal origin for giant Hamersley iron oxide ore bodies. Geology 27:175–178

Rosière CA, Rios FJ (2004) The origin of hematite in high-grade iron ores based on infrared microscopy and fluid inclusion studies: the example of the Conceição Mine, Quadrilátero Ferrífero, Brazil. Econ Geol 99:611–624

Rosière CA, Siemes H, Quade H, Brokmeier HG, Jansen EM (2001) Microstructures, textures and deformation mechanisms in hematite. J Struct Geol 23:1429–1440

Rosière CA, Baars FJ, Seoane JCS, Lobato LM, Silva LL, Souza SRC, Mendes GE (2006) Structure and iron mineralisation of the Carajás province. Trans Inst Mining Metall Sect B 115:B126–B136

Rosière CA, Spier CA, Rios FJ, Suckau VE (2008) The itabirites of the Quadrilátero Ferrífero and related high-grade iron ore deposits: an overview. Rev Econ Geol 15:223–254

Rosière CA, Sanglard JCD, Santos JOS, Mcnaughton N, Fletcher IR, Suckau VE, Spier CA (2012) Structural control and age of the high-grade iron ore of the Quadrilátero Ferrífero, Brazil. In: Peruvian Geological Congress and SEG 2012 Conference. Lima, Peru

Rouxel OJ, Dobbek N, Ludden J, Fouquet Y (2003) Iron isotope fractionation during oceanic crust alteration. Chem Geol 202:155–182

Rouxel OJ, Bekker A, Edwards KJ (2005) Iron isotope constraints on Archean and Paleoproterozoic ocean redox state. Science 307:1088–1091

Sampaio GMS, Pufahlb PK, Raye U, Kyser KT, Abreu AT, Alkmim AR, Nalini HA Jr (2018) Influence of weathering and hydrothermal alteration on the REE and δ^{56}Fe composition of iron formation, Cauê Formation, Iron Quadrangle, Brazil. Chem Geol 497:27–40

Santiago ESB (2016) Trace elements (in situ LA-ICP-MS) and stable isotopes (Δ^{33}S, Δ^{34}S, δ^{56}Fe, and δ^{18}O) in magnetite and sulphides: origin and evolution of the Neoarchean and Paleoproterozoic Cu-Au systems from the Carajás mineral province, Brazil. Unpublished PhD thesis, Universidade de Campinas

Santos JOS (2003) Geotectônica dos Escudos das Guianas e Brasil-Central. In: Bizzi LA, Schobbenhaus C, Vidotti RM, Goncalves JH (eds) Geologia, Tectônica e Recursos Minerais do Brasil. Companhia de Pesquisa e Recursos Minerais - CPRM. Brasília, Brazil, pp 169–226

Santos JOS, Lobato LM, Figueiredo e Silva RC, Zucchetti M, Fletcher IR, McNaughton NJ, Hagemann SG (2010) Two Statherian hydrothermal events in the Carajás province: evidence from Pb-Pb SHRIMP and Pb-Th SHRIMP dating of hydrothermal anatase and monazite. In: 7th South American Symp Isotope Geology (SSAGI), Brasília, Brazil

Saunier G, Pokrovski GS, Poitrasson F (2011) First experimental determination of iron isotope fractionation between haematite and aqueous solution at hydrothermal conditions. Geochim Cosmochim Acta 75:6629–6654

Schoenberg R, Marks MAW, Schuessler JA, von Blanckenburg F, Markl G (2009) Fe isotope systematics of coexisting amphibole and pyroxene in the alkaline igneous rock suite of the Ilímaussaq Complex, South Greenland. Chem Geol 258:65–77

Severmann S, Johnson CM, Beard BL, German CR, Edmonds HN, Chiba H, Green DRH (2004) The effect of plume processes on the Fe isotope composition of hydrothermally derived Fe in the deep ocean as inferred from the Rainbow vent site, Mid-Atlantic Ridge, 36°14'N. Earth Planet Sci Lett 225:63–76

Shanks WCP III (2014) Stable isotope geochemistry of mineral deposits. Treatise on Geochemistry 13:59–85

Sharp Z (1990) A laser-based microanalytical method for the in situ determination of oxygen isotope ratios of silicates and oxides. Geochim Cosmochim Acta 54:1353–1357

Skulan JL, Beard BL, Johnson CM (2002) Kinetic and equilibrium Fe isotope fractionation between aqueous Fe(III) and hematite. Geochim Cosmochim Acta 66:2995–3015

Sossi PA, O'Neill HS (2017) The effect of bonding environment on iron isotope fractionation between minerals at high temperature. Geochim Cosmochim Acta 196:121–143

Steinhoefel G, Horn I, von Blanckenburg F (2009) Microscale tracing of Fe and Si isotope signatures in banded iron formation using femtosecond laser ablation. Geochim Cosmochim Acta 73:5343–5360

Steinhoefel G, von Blanckenburg F, Horn I, Konhauser KO, Beukes NJ, Gutzmer J (2010) Deciphering formation processes of banded iron formations from the Transvaal and the Hamersley successions by combined Si and Fe isotope analysis using UV femtosecond laser ablation. Geochim Cosmochim Acta 74:2677–2696

Taylor D, Dalstra HJ, Harding AE, Broadbent GC, Barley ME (2001) Genesis of high-grade hematite orebodies of the Hamersley province, Western Australia. Econ Geol 96:837–873

Teixeira NL, Caxito FA, Rosière CA, Pecoits E, Vieira L, Frei R, Sial AN, Poitrasson F (2017) Trace elements and isotope geochemistry (C, O, Fe, Cr) of the Cauê iron formation, Quadrilátero Ferrifero, Brazil: Evidence for widespread microbial dissimilatory iron reduction at the Archean/Paleoproterozoic transition. Precambrian Res 298:39–55

Teng FZ, Dauphas N, Helz RT (2008) Iron isotope fractionation during magmatic differentiation in Kilauea Iki Lava Lake. Science 320:1620–1622

Thomazo C, Ader M, Farquhar J, Philippot P (2009) Methanotrophs regulated atmospheric sulfur isotope anomalies during the Late Archean (Tumbiana Formation, Western Australia). Earth Planet Sci Lett 279:65–75

Thorne WS, Hagemann SG, Barley M (2004) Petrographic and geochemical evidence for the hydrothermal evolution of the North deposit, Mt. Tom Price, Western Australia. Miner Deposita 39:766–783

Thorne WS, Hagemann SG, Webb A, Clout J (2008) Banded iron formation-related iron ore deposits of the Hamersley province, Western Australia. Rev Econ Geol 15:197–221

Thorne WS, Hagemann SG, Vennemann T, Oliver N (2009) Oxygen isotope compositions of iron oxides from high-grade BIF-hosted iron ore deposits of the central Hamersley Province, Western Australia. Constraints on the evolution of hydrothermal fluids. Econ Geol 104:1019–1035

Troll VR, Weis FA, Jonsson E, Andersson UB, Majidi SA, Högdahl K, Harris C, Millet M-A, Chinnasamy SS, Kooijman E, Nilsson KP (2019) Global Fe–O isotope correlation reveals magmatic origin of Kiruna-type apatite-iron-oxide ores. Nature Comm 10:1712. https://doi.org/10.1038/s41467-019-09244-4|www.nature.com/naturecommunications11234567890

Tsikos H, Matthews A, Yigal E, Moore JM (2010) Iron isotopes constrain biogeochemical redox cycling of iron and manganese in a Palaeoproterozoic stratified basin. Earth Planet Sci Lett 298:125–134

Urban N, Stribrny B, Lippolt HJ (1992) Iron and manganese deposits of the Urucum District, Mato Grosso do Sul, Brazil. Econ Geol 87:1375–1392

Veizer J, Ala D, Azmy K, Bruckschen P, Buhl D, Bruhn F, Carden GA, Diener A, Ebneth S, Godderis Y (1999) $^{87}Sr/^{86}Sr$, $\delta^{13}C$ and $\delta^{18}O$ evolution of Phanerozoic seawater. Chem Geol 161:59–88

Viehmann S, Bau M, Bühn B, Dantas EL, Andrade FR, Walde DN (2016) Geochemical characterisation of Neoproterozoic marine habitats: evidence from trace elements and Nd isotopes in the Urucum iron and manganese formations, Brazil. Precambrian Res 282:74–96

Walde DHG, Hagemann SG (2007) The Neoproterozoic Urucum/Mutún Fe and Mn deposits in W-Brazil/ SE-Bolivia: assessment of ore deposit models. Zdt Ges Geowiss 158:45–55

Walde DHG, Gierth E, Leonardos OH (1981) Stratigraphy and mineralogy of the manganese ores of Urucum, Mato Grosso, Brazil. Geol Rundsch 3:1077–1085

Wang Y, Zhu X-K, Mao J-W, Li Z-H, Chen Y-B (2011) Iron isotope fractionation during skarn-type alteration: A case study of Xinqiao Cu-S-Fe-Au deposit in the Middle-Lower Yangtze valley. Ore Geol Rev 43:194–202

Wawryk CM, Foden JD (2015) Fe-isotope fractionation in magmatic-hydrothermal mineral deposits: a case study from the Renison Sn-W deposit, Tasmania. Geochim Cosmochim Acta 150:285–298

Webb AD, Dickens GR, Oliver NHS (2004) Carbonate alteration of the Upper Mount McRae Shale beneath the martite-microplaty hematite ore deposit at Mount Whaleback, Western Australia. Mineral Deposita 39:632–645

Weis FA (2013) Oxygen and iron isotope systematics of the Grängesberg mining district (GMD), central Sweden. Unpublished PhD thesis, Uppsala Universitet

Weis FA, Troll VR, Jonsson E, Högdahl K, Barker A, Harris C, Millet MA, Nilsson KP (2013). Iron and oxygen isotope systematics of apatite-iron-oxide ores in central Sweden. In: Proceedings of the 12th Biennial SGA Meeting, vol 4, Mineral deposit research for a high-tech world. Uppsala, Sweden, pp 1675–1678

Weyer S (2008) What drives iron isotope fractionation in magma? Science 320:1600–1601

Whitehouse MJ, Fedo CM (2007) Microscale heterogeneity of Fe isotopes in >3.71 Ga banded iron formation from the Isua greenstone belt, southwest Greenland. Geology 35:719–722

Williams PJ, Barton MD, Johnson DA, Fontboté L, Haller A, Mark G, Oliver NHS, Marschik R (2005a) Iron oxide copper-gold deposits: Geology, space-time distribution, and possible modes of origin. Soc Econ Geol 100th Anniv Vol, pp 371–405

Williams HM, Peslier AH, McCammon C, Halliday AN, Levasseur S, Teutsch N, Burg JP (2005b) Systematic iron isotope variations in mantle rocks and minerals: the effects of partial melting and oxygen fugacity. Earth Planet Sci Lett 235:435–452

Yapp CJ (1990a) Oxygen isotopes in iron (III) oxides: 1 Mineral-Water Fractionation Factors. Chem Geol 85:329–335

Yapp CJ (1990b) Oxygen isotopes in iron (III) oxides: 2. Possible constraints on the depositional environment of a Precambrian quartz-hematite banded iron formation. Chem Geol 85:337–344

Zheng YF (1993) Calculation of oxygen isotope fractionation in anhydrous silicate minerals. Geochim Cosmochim Acta 57:1079–1091